Monthly Notices of the ROYAL ASTRONOMICAL SOCIETY

MNRAS **514,** 535–554 (2022) https://doi.org/10.1093/mnras/stac1148
Advance Access publication 2022 April 28

The importance of X-ray frequency in driving photoevaporative winds

Andrew D. Sellek ,[1]★ Cathie J. Clarke[1] and Barbara Ercolano[2,3]

[1]*Institute of Astronomy, University of Cambridge, Madingley Road, Cambridge CB3 0HA, UK*
[2]*Universitats-Sternwarte, Ludwig-Maximilians-Universität München, Scheinerstr. 1, D-81679 Müunchen, Germany*
[3]*Excellence Cluster Origins, Boltzmannstrasse 2, D-85748 Garching bei München, Germany*

Accepted 2022 April 22. Received 2022 April 21; in original form 2022 January 31

ABSTRACT

Photoevaporative winds are a promising mechanism for dispersing protoplanetary discs, but so far theoretical models have been unable to agree on the relative roles that the X-ray, extreme ultraviolet or far-ultraviolet play in driving the winds. This has been attributed to a variety of methodological differences between studies, including their approach to radiative transfer and thermal balance, the choice of irradiating spectrum employed, and the processes available to cool the gas. We use the MOCASSIN radiative transfer code to simulate wind heating for a variety of spectra on a static density grid taken from simulations of an EUV-driven wind. We explore the impact of choosing a single representative X-ray frequency on their ability to drive a wind by measuring the maximum heated column as a function of photon energy. We demonstrate that for reasonable luminosities and spectra, the most effective energies are at a few 100 eV, firmly in the softer regions of the X-ray spectrum, while X-rays with energies ∼1000 eV interact too weakly with disc gas to provide sufficient heating to drive a wind. We develop a simple model to explain these findings. We argue that further increases in the cooling above our models – for example due to molecular rovibrational lines – may further restrict the heating to the softer energies but are unlikely to prevent X-ray heated winds from launching entirely; increasing the X-ray luminosity has the opposite effect. The various results of photoevaporative wind models should therefore be understood in terms of the choice of irradiating spectrum.

Key words: radiative transfer – protoplanetary discs – circumstellar matter – X-rays: stars.

1 INTRODUCTION

Though first proposed to explain the long lifetime of H II regions around massive stars by resupplying them with material (e.g. Hollenbach et al. 1994), photoevaporative winds are now one of the most-promising mechanisms for dispersing protoplanetary discs (Ercolano & Pascucci 2017; Kunitomo, Suzuki & Inutsuka 2020) and thus ending the era of planet formation around a young star. The major successes of photoevaporative models include clearing discs from inside-out (Koepferl et al. 2013); the production of the so-called 'two-time-scale' behaviour (as opposed to the gradual power law decline of a purely viscous model, Hartmann et al. 1998) in which this dispersal is rapid due to the action of the UV-switch (Clarke, Gendrin & Sotomayor 2001), though some relic discs may remain (Owen, Ercolano & Clarke 2011; Owen, Clarke & Ercolano 2012); and reproducing the dependence of inner disc lifetime on stellar mass (Komaki, Nakatani & Yoshida 2021; Picogna, Ercolano & Espaillat 2021).

Photoevaporative winds are thermally launched: they occur when the upper layers of a disc become heated by high-energy radiation from either the central star (*internal* photoevaporation) or a massive neighbour (*external* photoevaporation) and the resulting pressure gradients drive material off of the disc. Broadly speaking, this is expected to happen for radii $r \gtrsim \frac{GM_*}{c_S^2}$ (for stellar mass M_* and sound speed in the wind c_S) where the available thermal energy is enough to overcome the gravitational potential of the star (Shu, Johnstone & Hollenbach 1993; Hollenbach et al. 1994; Font et al. 2004; Alexander et al. 2014; Clarke & Alexander 2016; Sellek, Clarke & Booth 2021). Equivalently, one can invert this to say that at a radius R, material must be heated above the escape temperature $T_{\rm esc} \sim \frac{GM_*\mu m_{\rm H}}{2k_{\rm B}R}$ (Owen et al. 2012).

In order to explain the ionized surroundings of massive stars, it was consequently natural for the earliest theories (Hollenbach et al. 1994) to assume the heating was due to the extreme ultraviolet (EUV) at energies $\gtrsim$ 13.6 eV. Though most stars are of a lower mass with lower temperature and UV fluxes, the derived mass-loss profile scaled with ionizing photon count (Φ) and so could be applied to solar mass stars by using a lower Φ value (Shu et al. 1993). However, without a strong contribution from the photospheric blackbody spectrum, the origin and magnitude of such an ionizing flux for low-mass stars is more debated and observationally challenging to determine due to absorption by hydrogen in the line of sight. Alexander, Clarke & Pringle (2004a) ruled out accretion hotpots as unable to produce a sufficient level of ionizing photons to drive a significant wind, while possible chromospheric activity is poorly understood. Nevertheless, the value of Φ can exceed solar levels (e.g. Gahm et al. 1979; Alexander, Clarke & Pringle 2005) with $10^{41}-10^{42}$ s^{-1} often assumed.

Ionizing radiation also extends into the X-ray, which is much easier to constrain in surveys (e.g. Preibisch et al. 2005; Güdel et al. 2007).

★ E-mail: ads79@cam.ac.uk

As a consequence, the relationship between X-ray luminosity L_X, spectrum shape and stellar properties is better understood. Its impact on the heating of winds was first assessed by Alexander, Clarke & Pringle (2004b), who concluded the mass-loss profiles were at best comparable to the EUV. However, X-rays drive winds from a larger area of the disc, potentially resulting in higher integrated mass-loss rates (Ercolano, Clarke & Drake 2009). Moreover, these winds were definitively X-ray driven: attenuating the EUV part of Ercolano et al. (2009)'s spectrum did not reduce their mass-loss rates since EUV photons cannot penetrate far into X-ray-driven winds (Ercolano & Owen 2010; Owen et al. 2012) which are typically denser (but slower) and more neutral than their EUV equivalents. They concluded softer X-rays < 1000 eV were particularly important as once they pre-screened their spectrum enough to absorb these, a significant wind could no longer be launched.

The important role for X-ray suggested by static models was corroborated by the hydrodynamical calculations of Owen et al. (2010, 2011, 2012), in which most of the material never even passes into the EUV-heated region. To make this calculation tractable, these works assumed thermal equilibrium with the temperatures prescribed as a pre-calculated function of density n and local X-ray flux L_X/r^2 via the ionization parameter $\xi = \frac{L_X}{nr^2}$ (Tarter, Tucker & Salpeter 1969). This equilibrium relationship was established using the MOCASSIN Monte Carlo radiative transfer code (Ercolano et al. 2003; Ercolano, Barlow & Storey 2005; Ercolano et al. 2008). The same methods, but with updated prescriptions that are also functions of the column density and use luminosity-dependent spectra, have been applied by Picogna et al. (2019, 2021) and Ercolano et al. (2021), with qualitatively similar results.

On the other hand, the work of Wang & Goodman (2017, hereafter WG17), which aimed to better understand the line spectra of the winds by including thermochemistry in the model, suggests EUV has the dominant role. The chemistry was handled using a simple chemical network of 24 species, with abundances updated according to reaction rates with each hydrodynamical time-step. Likewise to avoid assumption of thermal equilibrium they directly calculated heating rates from ray tracing – for simplicity using just four bins spanning the FUV, EUV, and X-ray – and cooling rates from a variety of molecular and atomic processes. These processes lead to a hotter, more tenuous, highly ionized, wind in which EUV photoionization and adiabatic cooling were the key elements of the thermal balance, suggesting that thermal equilibrium cannot be assumed. Moreover, the X-rays were seemingly important only for helping puff up the underlying disc with molecular cooling processes responsible for offsetting their heating. The FUV was likewise important to the heating in these underlying layers. The overall mass-loss rates were below those of X-ray models (e.g. Owen et al. 2012).

However, Nakatani et al. (2018b) performed a similar exercise but found instead that at solar metallicity thermal winds were mostly FUV-driven, with X-rays assisting mainly by increasing ionization levels, thus allowing FUV to penetrate more deeply. In the absence of FUV, X-rays did not drive a wind in these models, regardless of the hardness of the X-ray spectrum.

The thermal state of the wind is important for understanding wind observable quantities such as line spectra (e.g. Font et al. 2004; Ercolano & Owen 2016; Ballabio, Alexander & Clarke 2020; Weber et al. 2020). For example, an X-ray wind would mean slower, cooler winds than in the EUV case, which manifests in the centroid shift and full width at half-maximum (FWHM) of collisionally excited lines (which are both functions of the sound speed in the wind); this is seen for the [O I] 6300 Å line (Ballabio et al. 2020). Since it is produced by a neutral species, such a line requires a relatively low level of wind ionization, which is not very consistent with an EUV model (Font et al. 2004) meaning that the observed lines have a more natural explanation if the wind is X-ray driven. Ercolano & Owen (2016) showed how this line could be produced by an X-ray-driven wind, although since such high temperatures are required for its production its luminosity nevertheless scales with the EUV luminosity. Moreover, the mass-loss rates have a key impact on demographic indicators of disc dispersal such as the $\dot{M}_{\rm acc}-M_{\rm disc}$ plane (Sellek, Booth & Clarke 2020; Somigliana et al. 2020), the properties of transition discs (e.g. Owen et al. 2011, 2012; Picogna et al. 2019; Ercolano et al. 2021) and the correlation of accretion rates and dispersal times with stellar properties (Ercolano et al. 2014; Flaischlen et al. 2021; Picogna et al. 2021). Therefore, it is important that we resolve the tensions between the different studies outlined above with respect to the most important heating and cooling mechanisms if we are to establish accurate predictions of observables from photoevaporative models.

We can summarise five key differences: (a) the treatment of radiative transfer, (b) the shape and resolution of the irradiating spectrum, (c) the atomic cooling processes included, (d) the inclusion of molecules and molecular cooling, and (e) the assumption (or lack thereof) of thermochemical equilibrium. Here, we wish to address the question of driving radiation by exploring the first three of these through irradiating the WG17 density grids using MOCASSIN setup to create the conditions in their simulations. Specifically this allows us to comment on the consistency between the Monte Carlo and ray tracing radiative transfer methods, vary the spectral bins to establish the efficacy of different X-ray bands, and estimate the contributions of different mechanisms to thermochemical balance.

The aim of this paper is to explore how the role of X-rays in driving photoevaporative winds depends on the spectrum of the X-rays employed. In order to investigate this issue we will first attempt to reproduce the results of WG17 using the X-ray spectrum employed in their work (i.e. 1000 eV X-rays). Following a description of our radiative transfer modelling framework and its differences from previous work (Section 2), we describe in Section 3 how choices in the treatment of optical line cooling impact different regions of the disc and wind and find those required in order to produce a similar temperature structure to WG17. This then equips us to examine in Section 4 how the temperature structure is modified when we change the X-ray spectrum. We show that a modest (factor of 2) reduction in the characteristic frequency of the X-ray results in a substantial (order of magnitude) increase in the column that can be heated by X-rays and that such a change inverts the conclusion of WG17 with regard to the relative importance of UV and X-rays in driving thermal disc winds. We also show how the result that X-ray heating is optimized at energies around 500 eV can be quantitatively well understood in terms of a simple analytic model of radiative balance between cooling processes and X-ray heating. In Section 5, we discuss the contributions of different mechanisms to thermochemical balance in order to critically assess the need to include molecular cooling and the validity of the equilibrium assumption. Finally, we present our conclusions and discuss the impact they might have on disc evolution in Section 6.

2 MODEL DESCRIPTION

2.1 Key differences between previous works

The methodology used by different photoevaporation studies has varied substantially: WG17 (and similarly Nakatani et al. 2018b) conducted radial ray tracing to calculate an attenuated flux in each

cell in their simulations using the optical depth provided by a range of photoreactions. This process ignores the potential for scattering of radiation, the diffuse EUV field produced by recombinations, and the ability of these processes to change the frequency of radiation. The diffuse EUV has typically been thought important to photoevaporation (Hollenbach et al. 1994) although this is somewhat debated (Tanaka, Nakamoto & Omukai 2013; Hollenbach 2017) and may depend on any assumed disc structure. However, it provides a relatively inexpensive way of estimating the radiation field, allowing them to avoid assuming thermal equilibrium but instead update the ionization states of material and perform photoionization heating after each hydrodynamical time-step. That is to say, the thermal evolution of the disc/wind material is calculated by operator splitting, with atomic and molecular heating/cooling in one substep, and the hydrodynamical terms – adiabatic cooling by PdV work and advection of thermal energy (hereafter collectively hydrodynamical cooling) – in the other.

On the other hand, most of the works favouring X-ray photoevaporation (Owen et al. 2010, 2011, 2012; Picogna et al. 2019, 2021; Ercolano et al. 2021) have been based on calculations using MOCASSIN (Ercolano et al. 2003, 2005, 2008), a Monte Carlo code which releases a number of packets of fixed energy into a fixed density grid at frequencies randomly sampled from the input spectrum. As the energy packets pass through cells they have an absorption probability; if absorbed the packet is re-emitted in a random direction at a frequency randomly sampled from the local emissivity. This process inherently conserves energy in the radiation packets and so it requires an assumption of thermal equilibrium between radiative heating and cooling processes – once the packets have passed through the grid, the radiative intensity can be estimated and the temperature and ionization in each cell are updated iteratively until they give local heating and cooling rates that are equal. This procedure is then iterated until the solution converges.

Since this process is computationally more expensive, it would be impractical to run this at each time-step of a hydrodynamical simulation. Instead, assuming X-ray dominates the heating, the usual procedure is to use precalculate a relationship between the temperature, density and X-ray flux of simulation cells via the ionization parameter ξ. This can then be used to calculate the temperatures in a hydrodynamical simulation at each step without performing radiative transfer each time. While originally the fluxes were based only on geometric dilution (Owen et al. 2010), attenuation can be accounted for by providing fits at a range of column densities (Picogna et al. 2019). Post-processing with MOCASSIN can then used to confirm the self-consistency of the resulting solution (Owen et al. 2010; Picogna et al. 2019). Although MOCASSIN has been benchmarked against known solutions for the thermal structure of various setups, this does not guarantee its accuracy for this particular problem, particularly given that it necessarily ignores hydrodynamic contributions to the thermal balance.

Another major methodological difference between previous works is the irradiating spectrum. The Ercolano et al. (2009) spectrum used by works from Owen et al. (2010) to Picogna et al. (2019) covers energies from 11.27 eV (i.e. just above the first ionization energy of C) to around 12 keV and is sampled by MOCASSIN to 1396 different energy bins. The spectrum is based on the coronal emission of RS CVn active binaries and has roughly similar luminosities in the EUV (13.6−100 eV) and X-ray (> 100 eV) bands.

Whereas, WG17 model the spectrum using just four bands at 7, 12, 25, and 1000 eV. Their spectrum, (which follows Gorti & Hollenbach 2009) is overall softer than that of Ercolano et al. (2009) in that it contains 6.25 times more energy in the EUV band relative to the X-ray, and the representative X-ray is also slightly softer than the average of the Ercolano et al. (2009) spectrum ($\int E_\nu H_\nu \mathrm{d}\nu / \int H_\nu \mathrm{d}\nu = 1086$ eV). However, this attempt to represent energies covering two orders of magnitude perhaps does not really cover the extremes (particularly the softer end) of the X-ray band. This begs the questions of both whether (a) using just the four bands to spanning the whole spectrum are sufficient to resolve the true behaviour and (b) if so whether these are a sensible choice. We note that Nakatani et al. (2018b) adopt an even softer spectrum where the X-ray luminosity is a further factor ∼3 lower compared to the EUV, and there is a considerably larger FUV luminosity.

Broadly speaking, both MOCASSIN and the simulations of WG17 contain a somewhat similar set of cooling processes; with the latter (and also Nakatani et al. 2018b) also including some molecular cooling (from collisionally excited rovibrational states of H_2, H_2O, OH, and CO, following Neufeld & Kaufman 1993) and hydrodynamical cooling (as discussed above). This common set includes cooling by collisionally excited Lyman α radiation from neutral hydrogen,[1] collisionally excited forbidden lines (CELs) of metal species, and dust-gas thermal accommodation.

However, the set of CELs used by MOCASSIN is by far the more extensive as it is based on data from CHIANTI (Dere et al. 1997; Landi et al. 2006) (though as noted by WG17, a few species including neutral sulfur are missing from its database), whereas WG17 include only a select few following Tielens & Hollenbach (1985); these are all relatively low-energy transitions in the IR[2] and so are excited at fairly low temperatures, making them the dominant coolants at the modest temperatures of a photodissociation region (PDR), which is an appropriate description of the underlying disc which is mostly penetrated only by FUV (Gorti & Hollenbach 2008). However, in hot, (partially) ionized regions at or above the wind base, a number of different lines in the optical may come into play, such as the [O I] 6300 Å & 6365 Å and the [S II] 4068 Å & 6718 Å/6731 Å doublet, many of which are important observational tracers of outflows from discs (Hartigan, Edwards & Ghandour 1995; Simon et al. 2016; Fang et al. 2018; Banzatti et al. 2019). Being higher energy transitions, these lines have higher excitation temperatures and cannot be excited in the colder disc, but become important once material reaches a few 1000 K: the optical lines tend to have both higher Einstein Coefficients, as well as imparting more energy per decay and so once excited can be highly effective coolants.

Moreover, WG17 include an escape probability treatment based on the optical depth of their lines following Kwan & Krolik (1981). This is important if one wants to correctly estimate the line centre flux of any lines which are optically thick, such as resonance lines; practically speaking, this is only of consequence here for the Lyman lines which are permitted transitions and so have a higher oscillator strength than the forbidden lines by several orders of magnitude. WG17 reduce their cooling rates in proportion to the escape probability, assuming that reabsorbed photons reheat the gas and do not cool it. However, to reheat the gas, a collisional de-excitation of the excited state formed by photon reabsorption would be required, and the densities are everywhere orders of magnitude below the critical density of the Lyman α transition ($\sim 3 \times 10^{12}$ cm^{-3}) so collisional destruction of Lyman α is rare (Dijkstra 2017). More realistically the Lyman radiation should still escape, either in the optically thin line

[1] MOCASSIN also treats Lyman β but this is everywhere subdominant to α.
[2] While WG17 included [O I] 6300 Å as a coolant, they only modelled the decay of photodissociated OH, rather than collisional excitation.

wings (via a double diffusive process whereby reabsorbed photons perform a random walk in frequency e.g. Avery & House 1968; Dijkstra 2017) or by being absorbed by dust and re-emitted at longer, optically thin, wavelengths (Cohen, Harrington & Hess 1984) and thus the cooling rate matches the optically thin case (Hollenbach & McKee 1979).[3] MOCASSIN therefore assumes that either way, this should not, ultimately, impede the cooling and does not reduce the cooling rates i.e. assumes the line is effectively optically thin. This means a key difference between the methods is that Lyman cooling is likely several orders of magnitude more effective in MOCASSIN than assumed by WG17.

A final difference to note is that the density grid used by WG17 uses a larger inner boundary of 2 au compared to the works favouring X-ray photoevaporation which use 0.33 au. This could potentially be important if there is significant attenuation of the EUV at $\lesssim 2$ au. Nakatani et al. (2018b), who use an inner boundary of 1 au, report that varying their inner boundary to as little as 0.1 au made little difference to the heating and ionization rates in the outer disc as there was not sufficient shielding by the inner regions of the disc and its atmosphere. However, while this is therefore unlikely to drive a difference between previous works, attenuation by material closer to the star than the inner boundary, for example, accretion columns, remains possible and could affect the spectrum irradiating the disc and wind (e.g. Alexander et al. 2004a).

2.2 Our models

We aim to carry out radiative transfer in MOCASSIN with conditions designed to replicate the approach of WG17 within its existing framework. In this section we set out the details of how we achieve this. Our simulations present are labelled in the form K_Cooling representing the combination of a certain spectrum 'K' with a certain cooling model. The temperatures are completely calculated by MOCASSIN using its iterative proceedure i.e. unlike some previous works (e.g. Owen et al. 2010), we do not fix them to dust temperatures from D'Alessio, Calvet & Hartmann (2001) at high-column densities. Each model was run for eight iterations with 10^9 photons and a final ninth iteration with 10^{10} photons, at which point they has all converged.

For each model, we irradiate the same density profile for the wind and underlying disc; to aid comparisons to WG17, we used the profile derived from their fiducial simulation. Since MOCASSIN only accepts Cartesian grids, we interpolated on to a non-uniform Cartesian grid (designed to provide more resolution at smaller radii, as with the logarithmic grid of WG17). The total grid is 321 × 321 cells, of which 97724, with radii spanning $r = 2-100$ au, are active. The density profile is shown in Fig. 1.

2.2.1 Spectra

For our fiducial model, we replicate the spectrum of WG17. We set the nearest frequency bin in MOCASSIN to have the same luminosity and all other bins to be zero. Note though that unlike in WG17, since the energy of the packets must be conserved, after interactions with atoms or dust the energy can be re-emitted in a different frequency bin so there will be secondary radiation at other energies. Since it follows WG17 we label this spectrum with the key **W**; its luminosity in each band is listed in Table 1. We note in particular that the X-ray luminosity L_X is similar to the median value from surveys of T Tauri stars (e.g. Preibisch et al. 2005; Güdel et al. 2007).

In Section 4, we also consider a number of other spectra, including one with no X-ray and only UV (**U**), several with softer X-ray energy (**S###** where ### is the energy in eV), and the Ercolano et al. (2009) spectrum FS0H2Lx1 (**E**), which is a continuous spectrum as opposed to the rest which were all discrete. The soft X-ray spectra have X-ray energies from 100 to 900 eV in steps of 100 eV. We normalize spectrum E to have the same EUV luminosity to control for the location of the ionization front; as a result it has higher FUV and X-ray luminosities than the other spectra. To allow us to isolate the effects of increased X-ray luminosity from X-ray spectral shape, we thus also consider discrete spectra with the X-ray luminosity enhanced by a factor 6.25 to match that of spectrum E (**X###**). All these spectra are also summarized in Table 1.

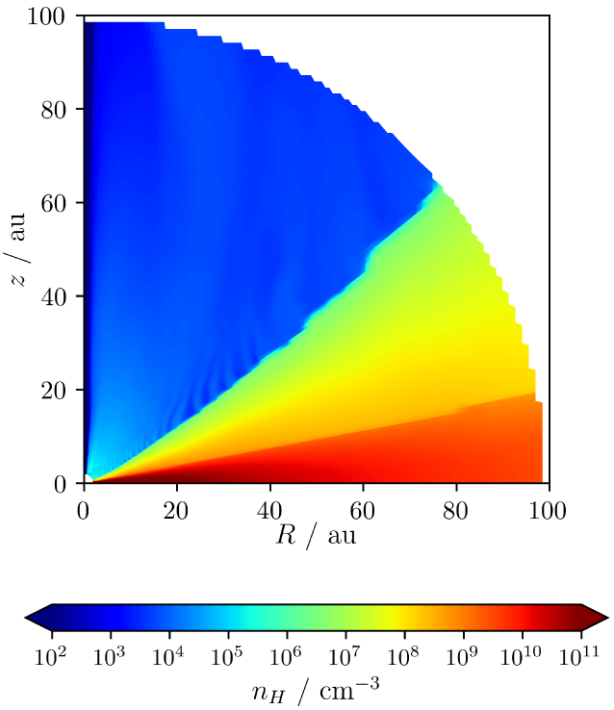

Figure 1. The interpolated density profile from WG17 used for our calculations with MOCASSIN.

2.2.2 Cooling

We present simulations for two cooling models which we also summarize in Table 2:

(i) **Full**, which includes all the mechanisms inherent to MOCASSIN. We also added atomic data for S I and the first 30 energy levels Fe II (enough to include the most accessible states) from CHIANTI (Dere et al. 1997, 2019) so that CEL radiation from these species is included, in particular, the transitions producing the [S I] 25 μm and [Fe II] 26 μm lines included by WG17 (though they only found the former to be particularly significant).

(ii) **IRFLNoH**, in which the only forbidden lines included are those longward of 10 μm in order to eliminate cooling from optical and near-infrared lines which were not modelled by WG17 and

[3] In reality, this is achieved at low densities by the cooling rate per excited atom being suppressed proportional to the escape probability but the excited population being increased in number in inverse proportion to the escape probability, resulting in no net effect; WG17 do not, however, suggest whether reabsorption affects their calculation of the coolant density.

Table 1. Luminosity by band and associated energy for each spectrum tested. Units are erg s^{-1}. The spectra are all discrete with a single energy bin per band (listed in brackets) except for E, which is continuous – in these cases the listed luminosity is that integrated over the range indicated.

Key Description	W Fiducial	U UV only	S### Soft X-ray	E Ercolano et al. (2009)	X### High L_X
Soft FUV	5.04×10^{31} (7 eV)	5.04×10^{31} (7 eV)	5.04×10^{31} (7 eV)	–	5.04×10^{31} (7 eV)
Lyman–Werner	3.07×10^{29} (12 eV)	3.07×10^{29} (12 eV)	3.07×10^{29} (12 eV)	1.6×10^{31} (11.27–13.6 eV)	3.07×10^{29} (12 eV)
EUV	2×10^{31} (25 eV)	2×10^{31} (25 eV)	2×10^{31} (25 eV)	2×10^{31} (13.6-100 eV)	2×10^{31} (25 eV)
X-ray	2.56×10^{30} (1000 eV)	–	2.56×10^{30} (### eV)	1.6×10^{31} (100–12000 eV)	1.6×10^{31} (### eV)

Table 2. Summary of cooling processes included in our cooling models versus WG17.

Process	Full	IRFLNoH	WG17
Lyman Alpha	Yes	No	Yes (escape probability)
Metal CELs	Yes	Yes (>10 μm only)	[C II] 158 μm, [O I] 63 μm, [S I] 25 μm, [Si II] 35 μm, [Fe I] 24 μm, [Fe II] 26 μm
Recombinations	Yes	Yes	Yes
Molecules	No	No	H_2, OH/H_2O and CO rovibrational

in which the cooling by the Lyman alpha and beta lines due to collisionally excited hydrogen is also turned off in order to mimic the attenuation of the line core.

Note that we expect the Full cooling to be a better representation of the physical reality, while the more restricted IRFLNoH is an exercise designed to bring the MOCASSIN treatment closer to that of WG17. Nevertheless, both models still exclude some processes – in particular molecular cooling and hydrodynamical cooling – which are not currently implemented within MOCASSIN. We discuss the potential impact of these in Section 5.

2.2.3 *Elemental abundances*

For the elements considered by WG17, we used the same abundances,[4] with all other elements set to zero. For the elements that overlap with Ercolano et al. (2009) (H, He, C, O, Si, S), these values are identical; in addition, WG17 include Fe but not N, Ne or Mg. There can be reasonably significant, observable, emission from the omitted elements: we tested the difference including them would make to our results, ultimately finding it made qualitatively little difference to the overall conclusion.

Assuming an atomic/ionic composition, the mean molecular weight μ of the gas can be calculated as

$$\mu = \frac{\sum_i m_i A_i}{\sum_i A_i + n_e/n_H}, \quad (1)$$

where m_i are the atomic masses relative to hydrogen, A_i are the atomic abundances relative to hydrogen and n_e/n_H is the ratio of the free electron density to the hydrogen density. For a neutral atomic gas of our adopted composition, $\mu = 1.287$, though the value can be somewhat lower in regions of significant ionization.

[4]He/H = 0.1, C/H = 1.4×10^{-4}, O/H = 3.2×10^{-4}, Si/H = 1.7×10^{-6}, S/H = 2.8×10^{-5}, and Fe/H = 1.7×10^{-7}.

2.2.4 *Dust*

We assume a single grain population of 5Å with the 'Car_90' composition from MOCASSIN's library of dust datafiles which represents a neutral carbon grain in the form of a PAH/graphitic solid, the closest available to the PAH assumption of (WG17).

3 EXAMPLE TEMPERATURE STRUCTURE

To provide context for our results, we first investigate whether our MOCASSIN calculations can reproduce the temperature structure found by WG17 when we employ the same input spectrum (i.e. EUV, FUV, and 1000 eV X-rays) and how this is impacted by the cooling rates. Therefore, in Fig. 2, we present the temperature structure in the simulations with spectrum W for the two different cooling models described in Section 2.2.2). Based on the penetration of different radiation, we can delineate the resulting temperature structure into three broad regions – the wind, the warm disc and the cold disc – which we discuss in turn before demonstrating how we use the temperatures to determine where a wind can be launched.

In the models of WG17, the wind and disc are divided by an ionization front (IF) where a sharp density contrast is seen (Fig. 1). The locations of our IFs agree well with WG17, indicating that the Monte Carlo radiative transfer solution by MOCASSIN is consistent with the ray tracing conducted by WG17 and suggestive of a self-consistent EUV-driven solution. This can be seen in terms of the penetration depth of EUV with the $\tau = 1$ surface marked in each case with the light dash–dotted line: being relatively close in frequency to the first ionization energies of hydrogen and helium, the EUV has the largest cross-section for photoionization and hence the smallest penetration column of $N_{H\,I} \sim 5 \times 10^{17}\,cm^{-2}$. The low densities of the EUV-driven wind, and its high levels of ionization, are key to allowing the EUV to reach this far, in contrast to the higher density X-ray-driven winds into which the EUV does not penetrate very far (Owen et al. 2012).

The wind region penetrated by the EUV is hot and approximately isothermal: for the Full cooling model at around 10^4 K and for the IRFLNoH cooling model at around 3×10^4 K. The latter model yields temperatures that are close (within around 30 per cent) to those obtained by WG17: this is as expected given that the model omits cooling processes also omitted by WG17.[5] On the other hand within

[5]We also tried to achieve agreement with the hot temperatures of WG17 by more measured means such as removing only (a) the Lyman lines, (b) certain metals or (c) even individual lines from the cooling, but only the IRFLNoH model combining several of these was able to produce the $\sim 3 \times 10^4$ K wind temperatures.

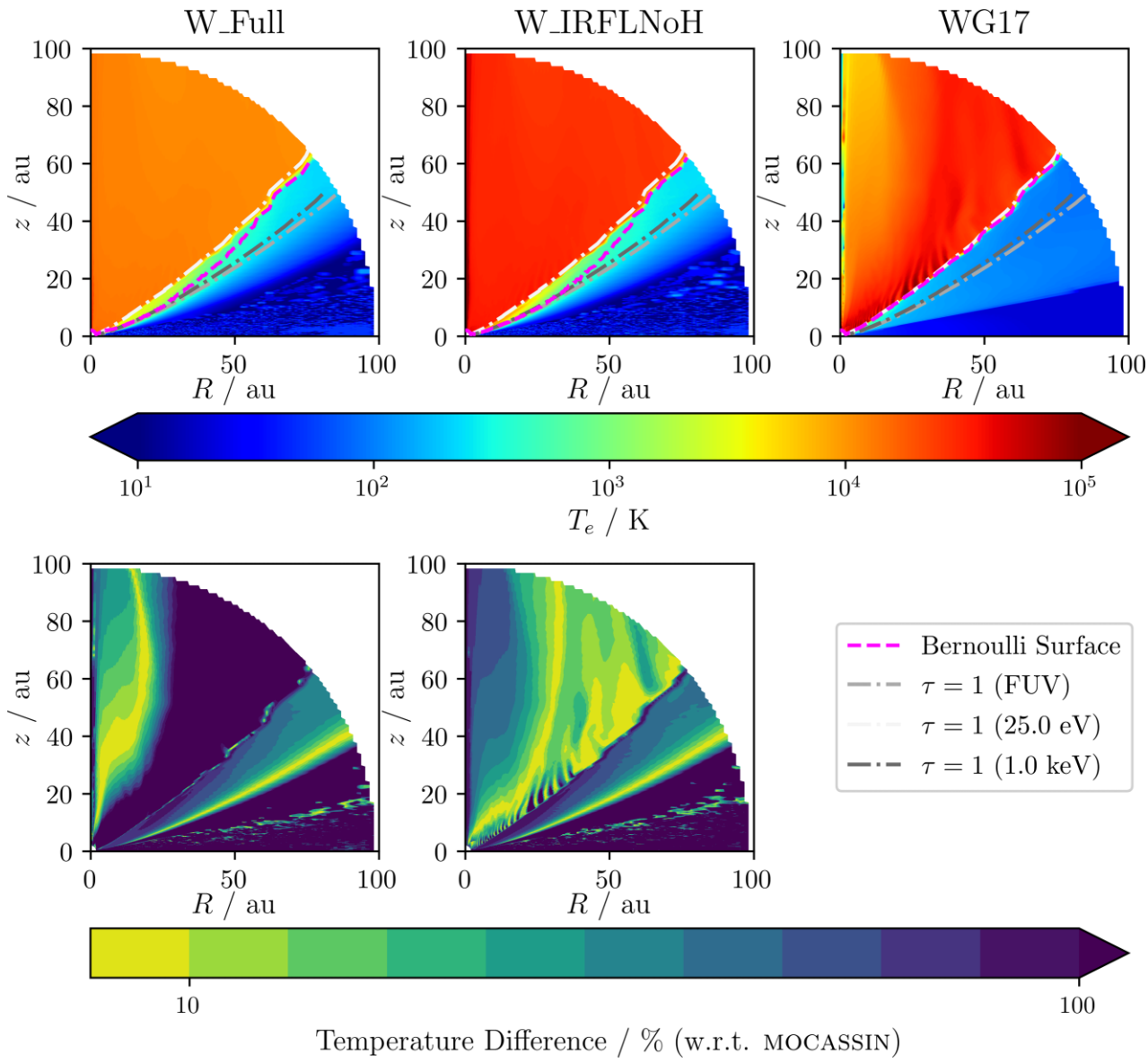

Figure 2. Comparison of the temperature structure obtained using MOCASSIN with that of WG17. The left-most column shows the full cooling model, while the central column shows the restricted 'IRFLNoH' model in which cooling from Lyman lines and optical/NIR collisionally excited lines are turned off. The top row shows the temperatures, while the second row illustrates the percentage difference between the fiducial model of WG17 and our simulations. In the bulk of the wind region, the IRFLNoH cooling model has smaller temperature differences as indicated by the lighter colours. The pink dashed line indicates the surface where the Bernoulli function becomes positive while the dot–dashed lines (clockwise from the z-axis) are the $\tau = 1$ surfaces for EUV, X-ray and FUV, respectively.

$R \lesssim 20$ au and at $z \gtrsim 20$ au, we see that WG17 find a cooler lobe of temperatures much closer to the 10^4 K of the Full Model. We suggest, in Section 5, that the origin of these cooler temperatures is adiabatic cooling which is neglected in our (radiative equilibrium) models.

While in principle hotter wind temperatures act to make the wind more highly ionized and therefore more transparent to radiation, we find little change in the location of the ionization front regardless of cooling and wind temperature. This is because the wind is primarily photoionized rather than thermally ionized so the hotter temperatures make little difference to the transparency of the wind. Moreover the penetration depths of the X-ray and FUV frequencies are sufficiently large that any modification to the neutral column in the EUV-heated wind region has negligible effect.

Beyond the ionization front, both of our simulations have broadly the same appearance. First, we come to a warm ~ 1000 K region heated by both FUV and X-ray. We see that this region is generally warmer than it was found to be by WG17 by a few 100 K; this implies our models either have some additional heating or are missing some cooling – we suggest in Section 5.3 that this is likely the result of molecular cooling. There is little difference between the cooling models as these temperatures are not generally warm enough to significantly excite the optical lines that are turned off in the IRFLNoH model.

The FUV has an opacity largely dominated by dust absorption,[6] and for the grains in question, can penetrate a column of roughly 2×10^{22} cm^{-2}, while the high-energy 1 keV X-rays can reach around

[6]Though there are also significant contributions from carbon and sulfur photoionization.

$10^{22}\,\mathrm{cm}^{-2}$. Therefore, the FUV and X-ray reach similar depths in this case. Beyond this point the temperatures appear to decline and tend towards better agreement with WG17. The mid-plane of the disc is dark to all the bands of radiation included. The MOCASSIN temperatures in this region are noisy due to low photon counts and the low temperature behaviour of the algorithm applied to find equilibrium.

In summary then, our IRFLNoH model, which turns off a number of atomic cooling channels, reasonably reproduces the temperature structure found by WG17, albeit with slightly warmer conditions below the ionization front.

For a given temperature profile, a wind can be launched wherever the material is hot enough to be unbound and overcome the gravitational potential Φ. This can be described in terms of the volume in which the Bernoulli parameter is positive (Liffman 2003; WG17)

$$B := \frac{v^2}{2} + \frac{\gamma}{\gamma - 1}\frac{P}{\rho} + \Phi > 0. \tag{2}$$

Since we do not solve the hydrodynamics, we cannot determine the velocities v for our simulations. However, we can assume that they are initially subsonic (Clarke & Alexander 2016; Sellek et al. 2021) at the base of the wind and so the poloidal kinetic energy term $v_\mathrm{p}^2/2$ is small compared to the thermal term P/ρ, while the azimuthal kinetic energy term $v_\phi^2/2 \sim \frac{\Phi}{2}$. Thus, we define the Bernoulli surface as the location where

$$T = T_\mathrm{Bern} := \frac{1}{5}\frac{GM_*\mu m_\mathrm{H}}{k_\mathrm{B} r} \approx 27600\,\mathrm{K}\left(\frac{r}{\mathrm{au}}\right)^{-1}\frac{\mu}{1.287}, \tag{3}$$

assuming that the wind is mainly atomic and so $\gamma = 5/3$ and where the typical value is given assuming a star of $1\,\mathrm{M}_\odot$. When assessing whether a given cell has a temperature above T_Bern, its local value of the mean molecular weight μ – calculated from the local ionization fraction as per equation (1) – is used. Up to a numerical factor, this is similar to the escape temperature formalism of Owen et al. (2012) (though see Picogna et al. 2021, for a discussion about how this does not completely accurately capture the temperature at the wind base).

The Bernoulli surface is plotted as the magenta dashed line on Fig. 2. In the case of WG17's temperature profile, it lies along the ionization front, coincident with the $\tau = 1$ surface of EUV. This is strongly indicative of an EUV-driven wind. In our simulations, for $R \gtrsim 50\,\mathrm{au}$, we also see a good agreement between these two, though the temperature gradient at this location is less sharp so there is a small difference. Within $10 - 50\,\mathrm{au}$, the Bernoulli surface dips down below the ionization front, implying that in our simulations, the combination of FUV and X-ray is capable of heating the material to a hot enough temperature to drive a wind (though only at relatively low columns and not all the way down to their $\tau = 1$ surfaces). In the IRFLNoH case, this dip extends to slightly smaller radii due to the reduced cooling around the higher inner-disc T_Bern. Viewed another way, the innermost limit is on the order of the gravitational radius $r_G = \frac{GM_*}{c_\mathrm{S}^2}$, which is smaller for the hotter wind temperatures.

Our MOCASSIN simulations with input spectrum matching that of WG17 thus produce thermal structures that corroborate the conclusion of WG17 that 1000 eV X-rays are not able to drive a wind from the outer disc regardless of any differences in cooling processes. In the inner disc, the simulations indicate a possible minor role for FUV/X-ray wind launching but the Bernoulli surface is only modestly below the ionization front. We are now in a position to assess how this conclusion is affected when we vary the input X-ray spectrum employed.

4 ROLE OF X-RAY FREQUENCY

Having understood how the chosen cooling models give rise to the temperature profiles, we wish to further elucidate the role that the X-rays are playing in our simulations, and examine the potential of different X-ray energies to drive a wind. In particular, we will seek the most effective radiation and so we are interested in whether there are X-ray bands that can heat a larger column than the EUV.

Therefore, as a control, we first run a pair of simulations with the X-rays removed that is UV-only (simulations U_Full and U_IRFLNoH) and present their temperature profiles in the first column of Fig. 3. Removal of X-rays makes fairly little difference to the overall picture of a 10^4 K (3×10^4 K) wind for the Full (IRFLNoH) cooling model. On the other hand, we see cooler temperatures below the ionization front, with the remaining heating provided mainly by FUV photoionization of carbon. The difference to the fiducial simulations confirms the role of X-ray in heating this region in those earlier models through photoionization of hydrogen and helium. Nevertheless while closer to those found by WG17, the temperatures are still a little too hot, strengthening the argument for missing coolants in that region (as opposed to say, uncertainties in X-ray heating efficiency). These temperatures are, however, sufficiently low that the Bernoulli surface no longer dips down but follows the ionization front at all radii. Therefore, at these luminosities, FUV alone is not able to drive a wind from below the ionization front. That said, a higher FUV luminosity (e.g. Nakatani et al. 2018a, b), different FUV spectrum, different assumptions about the nature of the dust, or inclusion of molecular heating (e.g. FUV pumping of H_2) may allow for more significant FUV heating (e.g. through the dust photoelectric effect), potentially sufficient to launch a wind. Exploring the role of FUV further is beyond the scope of this work.

Now, we proceed to vary the frequency of the radiation band from 100 to 900 eV in steps of 100 eV. The aim of this exercise is to determine the impact of using a single band – and correspondingly the choice of its energy – on X-ray driving of winds. We thus keep the luminosity constant while doing so.

In the second column of Fig. 3, we depict the temperature structure for the runs with 500 eV which present the largest contrast with the 1 keV results discussed hitherto. For both of our cooling models, X-rays of this energy are clearly able to heat material comfortably below the ionization front to escape and thus drive a wind from all radii. It is therefore clear that the choice of X-ray frequency is a key parameter affecting whether X-rays can heat material beyond the EUV ionization front sufficiently to drive a wind.

4.1 Which radiation is most effective?

To illustrate which X-ray bands can effectively heat a larger column than the EUV, we plot in Fig. 4 the neutral hydrogen column density to the Bernoulli surface achieved by each energy for our S### simulations. We show this dependence for four different radii as the solid lines. In addition, the triangles of corresponding colour (plotted at 25 eV) mark the column at the Bernoulli surface at the same radii in our UV-only simulations and the circles (plotted at 1000 eV) likewise for WG17's fiducial model.

Above around 800 eV, we see that at large radii, the X-rays cannot heat a greater column than the EUV. Moreover, for all radii, at the lowest energies, the column heated by the X-ray is not much greater than the EUV as these frequencies are quite strongly absorbed. The most effective choices for a single X-ray energy that will heat the largest column are those in the range $500 - 700$ eV, depending slightly on the radius in question. We explore the shape of these

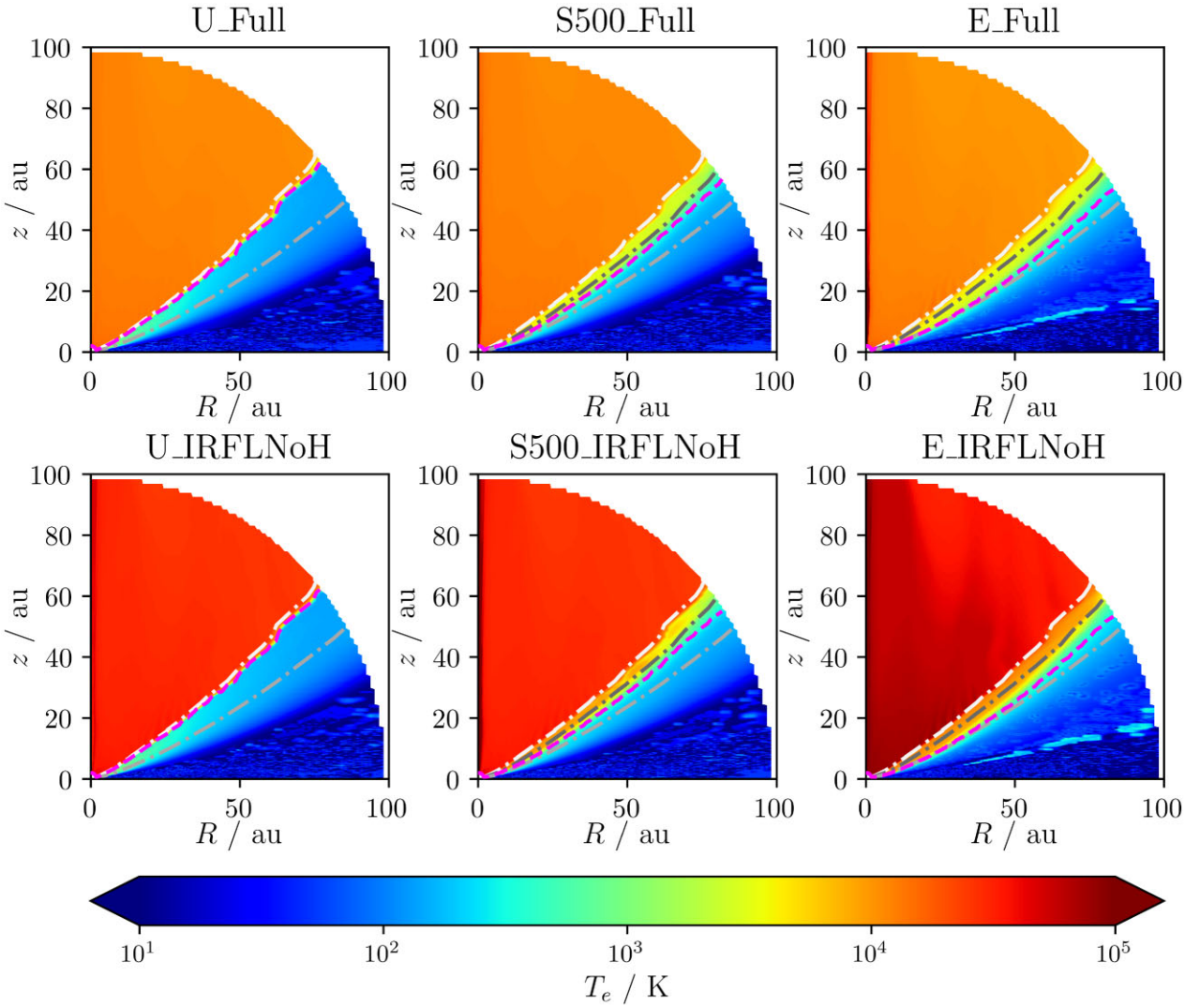

Figure 3. Comparison of the temperature structure obtained for different combinations of spectra and cooling model. From the left- to right-hand panels: the UV-only spectrum, a spectrum with 500 eV X-ray and the spectrum of Ercolano et al. (2009). In each case, the pink dashed line indicates the surface where the Bernoulli function becomes positive while the dot–dashed lines represent $\tau = 1$ surfaces for EUV, 500 eV X-ray and FUV.

curves with a simple model in Section 4.2, illustrated here with the black-dashed line (equation 7 for a fiducial value of $\epsilon_c = 10^{-22}$ cm^2). Note that since we control L_X, although in each case our spectrum is a effectively a delta function, Fig. 4 also in effect gives the relative contribution in a flat spectrum where each band has luminosity of 2.56×10^{30} erg s^{-1}. For now, we will proceed to discuss these as individual choices (i.e. as delta function spectra attempting to capture the whole spectrum), but will return in Section 4.4 to examine the effect of a realistic spectral shape in determining what is genuinely representative.

The choice of cooling model makes fairly little qualitative difference to these results; in part because the cooling rates between them are not so different for typical values of $T_{\rm Bern}$. The biggest difference between the two panels of Fig. 4 is seen for 7 au where $T_{\rm Bern}$ is high enough for the omission or inclusion of atomic cooling channels to affect the temperature attained. In either case, an X-ray-driven wind can be launched here and given the modest contribution to the total wind mass-loss rate from such small radii, the correct treatment of optical forbidden line cooling and Ly α (and β) cooling is not an important factor in determining X-ray driven mass-loss.

Instead, we conclude that the limited role for X-rays relative to UV in the simulations of WG17, predominantly reflects the fact that 1000 eV X-rays are too hard – and so interact too weakly with the disc gas – to heat it sufficiently to drive a wind on their own, regardless of the differences in cooling processes. That said, in absolute terms, the columns at the base in the simulations by WG17 are only $2-8 \times 10^{19}$ cm^{-2}. Whereas, despite the Bernoulli surface in our UV-only simulations lying very close to that of WG17, the column at an equivalent radius can be up to $\sim$10 times higher at $1-5 \times 10^{20}$ cm^{-2}. The origin of this behaviour is that the temperature gradient is shallower in our UV-only simulations because they are hotter below the base than found by WG17. Thus, the Bernoulli temperature is reached at a slightly lower height, below the IF. However, since the base is only mildly flared, photons reach it at a very glancing angle – the distance travelled below the WG17 IF at $n_{\rm H\,I} \sim 10^6$ cm^{-3} is thus considerable.

We cannot directly measure mass-loss rates from our models as we have not performed hydrodynamic simulations to adapt the density and velocity fields to be consistent with our different temperatures. However, since the amount of mass-loss determines how much

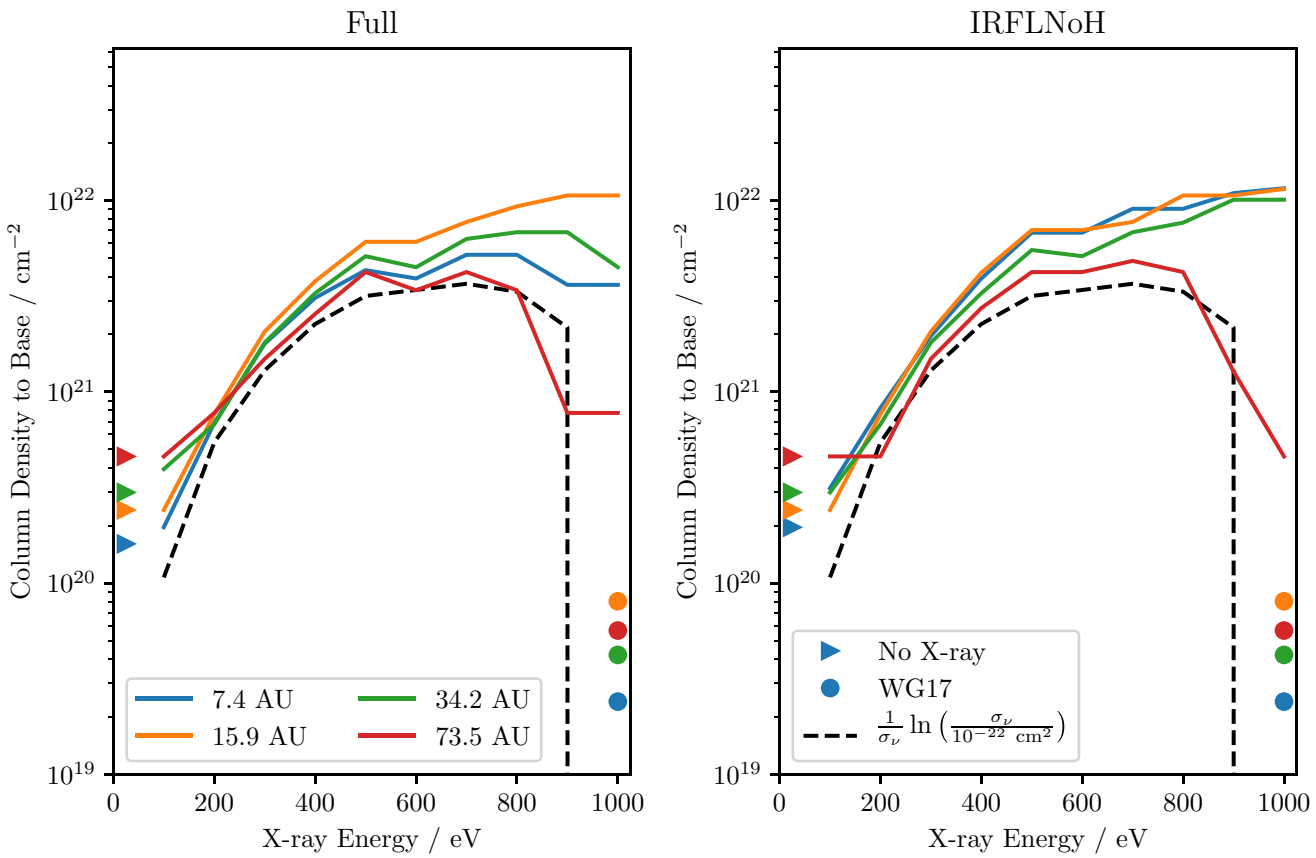

Figure 4. The H I column to the Bernoulli surface for each energy of X-ray at selected radii (solid lines). Simulations with the Full cooling model are shown on the left-hand panel and the IRFLNoH cooling on the right-hand panel. In each case, the triangles and circles represent the corresponding values for the UV-only spectrum and WG17's temperature field, respectively. The dashed line is equation (7) for $\epsilon_c = 10^{-22}$ cm^2.

material the radiation has to pass through to reach the wind base, it is reasonable to assume that $\dot{M} \propto N$ (i.e. we are assuming that $N \propto n_{\rm base}$ and $\dot{M} \propto n_{\rm base}$). Therefore, we would expect the higher columns in the UV-only simulations to translate into a similar factor ∼10 boost in the mass-loss rates. We ascribe this difference to additional cooling in the model of WG17; indeed, when they produced a setup closer to Owen et al. (2010) (their OECA analog) by turning off some of this cooling, they did see a mass-loss rate that was higher by a factor of 4−5. Note that since in the outer disc, which typically dominates the mass-loss rates, X-rays cannot heat a larger column than EUV, we would expect the mass-loss rates of a 1000 eV X-ray simulation to be only marginally higher than an UV-only one, as observed by WG17.

In this context, we estimate that if one wishes to use a single energy to represent the X-rays, moving to ∼ 500 ev would increase the mass-loss rate by a factor of ∼4−6 over that found in a simulation driven by UV-only. As we will discuss further in Section 4.4, the shape of the spectrum controls whether such energies are present in sufficient numbers to be representative.

4.2 Explanatory model

As discussed before, we assume that a wind is launched when gas is heated above $T_{\rm Bern}$ (equation 3). We now consider a toy model for whether monochromatic X-ray radiation of frequency ν can launch a wind on its own.

Assuming that all X-ray radiation absorbed goes into heating the gas, the heating rate per unit volume can be written in terms of the geometrically diluted and attenuated X-ray flux, F_X ($= \frac{L_X}{4\pi r^2} e^{-N\sigma_\nu}$), local gas density, n and photoionization cross-section, σ_ν, as $F_X n \sigma_\nu$. We assume that σ_ν is independent of temperature since the gas is predominantly photoionized rather than thermally ionized.[7]

However, it is important to note that this form for the heating is an overestimate. First, it neglects the fact that some of the energy is used up in overcoming the ionization energy of the electrons; for X-ray ionization of hydrogen (and to a lesser extent helium) this is only a small correction $\lesssim$ 10 per cent, but could be more significant for metals such as oxygen, where inner shells have ionization energies in the 100s of eV. Moreover, it neglects further losses due to secondary ionization by the Auger effect in the heavier elements, and similarly the possibility of that the energy carried by the photoelectron may be lost to further ionizations or collisional excitation before it can thermalize (e.g. Maloney, Hollenbach & Tielens 1996). On the other hand, MOCASSIN treats the X-ray heating more self-consistently, accounting for losses to secondary ionization and excitation as a function of ionization fraction using the fits of Shull & van Steenberg (1985); for high levels of ionization, the chance of thermalizing through electron–electron collisions becomes greater than the chance

[7]In practice, the cross-section will depend somewhat on temperature, since the ionization state of the absorbing material depends on the recombination coefficient α which is temperature dependent.

of ionizing or exciting neutral hydrogen, so the heating fraction $f_X \rightarrow 1$. However, in gas with a largely atomic composition, it can be on the order of 10 per cent. Hence, we will scale the heating term in our thermal balance by f_X.

The predominant cooling effects are two-body processes, requiring a collisional excitation between an electron or neutral and an ion or neutral – assuming these are below their critical densities (above which collisional de-excitation dominates over radiative de-excitation), the cooling rate per unit volume for each can be written as $n^2\Lambda_{n,i}(T)$ (where the subscript n here indicates that Λ is per particle per number density), and hence the total cooling rate is of the same form $n^2\Lambda_n(T)$ ($\Lambda_n(T) = \sum_i \Lambda_{n,i}(T)$).

Assuming thermal equilibrium, we may set the heating and cooling to equal, and rearrange to find

$$\Lambda_n(T) = \frac{f_X}{4\pi}\frac{L_X}{nr^2}\sigma_\nu e^{-N\sigma_\nu} = \frac{f_X\xi}{4\pi}\sigma_\nu e^{-N\sigma_\nu}, \tag{4}$$

where we can identify the ionization parameter $\xi = \frac{L_X}{nr^2}$ (Tarter et al. 1969; Owen et al. 2010). We thus see that the relationship between the ionization parameter and temperature depends on the column density at the material N (Picogna et al. 2019) as well as the frequency of radiation involved (cf. the spectral shape Ercolano et al. 2021).

A simple consequence of equation (4) is that assuming $\Lambda(T)$ is a monotonically increasing function of T, the highest temperatures at a given column are produced by that radiation, across all frequencies, for which $\tau = N\sigma_\nu = 1$. More energetic radiation is more deeply penetrating so is simply not absorbed well enough locally to deposit much energy into the material. Conversely, less energetic radiation is more easily absorbed and so has been too strongly attenuated by the time is reaches the column N. One can thus replace the frequency-dependent terms with an 'efficiency' (with dimensions of a cross-section) for a given frequency of radiation:

$$\sigma_\nu e^{-N\sigma_\nu} \rightarrow \epsilon_\nu. \tag{5}$$

Note that while we here call this the efficiency, other works refer to f_X using the same name; in practice both determine the ability of the X-rays to heat the gas and effects such as overcoming the ionization energy will mean that the real efficiency $< \sigma_\nu e^{-N\sigma_\nu}$. The constraints on cross-sections capable of heating that we now proceed to derive are only strengthened by these effects.

The requirement that $T \geq T_{\rm Bern}$ in the wind gives us a requirement on the minimum efficiency of the X-rays[8]

$$\epsilon_\nu \geq \epsilon_c := \frac{4\pi\Lambda_n(T_{\rm Bern})}{f_X\xi}. \tag{6}$$

Given the X-ray luminosity L_X, stellar mass M_*, radius r, local density n, and information about the ionization states of each element (which controls $\Lambda(T)$ and f_X), we can determine a value for ϵ_c at each location in the density field. Note that the X-ray luminosity, cooling rate and heating fraction are degenerate in their effects on ϵ_c, and so each may be changed to similar effect. We discuss them each in more depth in Sections 4.3, 5.3, and 5.4, respectively.

From the definition of the efficiency, we can solve for the maximum column that radiation of a single frequency can heat to the required temperature

$$N_{\rm max} = \frac{1}{\sigma_\nu}\ln\left(\frac{\sigma_\nu}{\epsilon_c}\right), \tag{7}$$

where we expect that unbound material should exist anywhere that $N < N_{\rm max}$.

A necessary but not sufficient condition is therefore that $N_{\rm max} > 0$, in which case our single choice of frequency must have $\sigma_\nu > \epsilon_c$ since otherwise even completely unattenuated radiation could not heat the wind. This imposes an upper bound on the X-ray energies that can heat the gas to the escape temperature. The highest column (at fixed ϵ_c) is heated by radiation with $\sigma_\nu = e\epsilon_c$, such that $N = 1/\sigma_\nu = 1/(e\epsilon_c)$. At larger still values of σ_ν, the column heated is moderately larger than $1/\sigma_\nu$ ($\tau \gtrsim 1$), but is nevertheless a decreasing function of σ_ν.

Note that correspondingly, the optical depth at the base is $\tau = 1$ for the most efficient radiation. Since they heat inefficiently, higher energies are likely to be optically thin at the base, while the lower energies will be somewhat optically thick. Therefore for radiation effective enough to drive an X-ray wind, we expect order unity optical depth at the base. Broadly speaking this means that the temperatures around the base are not declining purely due to increasing cooling from denser material but also by a decrease in heating as the radiation is attenuated too. The decrease in heating is the more important effect once $\tau > \frac{N}{nd}$ ($\sim$0.4–0.5 below the base) where $\mathrm{d} = n/\frac{\partial n}{\partial r}$. This means that an optically thin prescription using a single ξ–T relation and assuming lower temperatures result only from lower densities (e.g. Owen et al. 2012) will generally be less accurate than an attempt to account for column density or attenuation of radiation.

4.2.1 Application to Results

We first examine which of the X-ray radiation bands can heat a larger column than UV alone, by evaluating ϵ_c equation (6) along the Bernoulli surface (i.e. the ionization front) in the ultra-violet only model; to allow for comparison to WG17, we use $L_X = 2.56 \times 10^{30}$ erg s^{-1}, and since EUV-heated gas is nearly completely ionized, we assume $f_X = 1$. We have argued that a necessary condition for effective X-ray heating below the ionization front is that $\sigma_\nu > \epsilon_c$, so if the values of ϵ_c correspond to cross-sections in the X-ray regime then we expect some X-rays to be potent sources of heating at – and therefore somewhat below – the UV-only wind base and hence an X-ray-driven wind to be possible.

Thus, Fig. 5 depicts the run of ϵ_c with radius along the Bernoulli surface in the UV-only model (Fig. 3) while the right-hand axis equates values of ϵ_c with the value of the X-ray photon energy for which $\sigma_\nu = \epsilon_c$, this being the maximum energy for which heating to $T_{\rm Bern}$ would be possible even in the case of no attenuation.

Except in the innermost parts of the disc, the values for ϵ_c derived are in the range 10^{-22}–10^{-21} cm^2 and reach a minimum around 10–20 au. These correspond to the photoionization cross-sections of photons in the range 400–1000 eV.[9] The shallow increase to larger radii is due to the effects of geometric dilution weakening the irradiating flux, though this is largely offset by the material being less tightly bound (with a lower $T_{\rm Bern}$ at which the cooling rates to be overcome are lower) and less dense.

[8]Note that since we assumed the cooling depends quadratically on density, the local density explicitly appears in this formula through ξ; however, if the density is sufficiently high for a linear dependence, our approach still works with a different definition of the cooling rate, and ϵ_c will become independent of n.

[9]To perform this calculation we assume a neutral gas and use the opacities of Verner & Yakovlev (1995), Verner et al. (1996); in practice, the cross-sections for photoionization are only weakly affected by ionization except in terms of the exact location of the ionization energy.

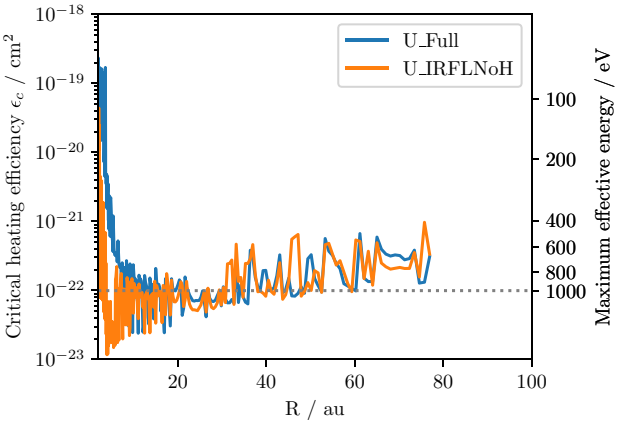

Figure 5. The critical efficiency required to overcome the local cooling along the Bernoulli surface in the U_Full (blue) and U_IRFLNoH (orange) simulations as a function of radius assuming $L_X = 2.56 \times 10^{30}$ erg s^{-1} (WG17) and $f_X = 1$. The right-hand axis calibrates this scale in terms of the X-ray energy with cross-section equal to this value – any higher energy will have too low a cross-section to achieve the required efficiency. The maximum energy that is effective on its own at this luminosity is similar between the cooling models except for the inner 20 au. In addition, 1000 eV - as used by WG17 - is marked with the dotted line for reference.

We would thus expect that over much of the disc outside $\gtrsim 40$ au, 1000 eV acting alone should not be able to launch an X-ray-driven wind, though it is marginally able to do so around ~ 20 au. Indeed, this is what was discussed in Section 3 and illustrated in Fig. 4. It is likely that in practice the ability of these harder X-rays to launch a wind was assisted by the presence of FUV which has a similar cross-section for absorption and thus is contributing to the heating at these columns.

On the other hand, energies $\lesssim 600$ eV should be able to launch an X-ray-driven wind from the entire disc as was the case for the 500 eV example shown in Fig. 3. The mild increase of ϵ_c with radius implies that the maximum energy for effective X-ray heating should decrease mildly with increasing radius. Assuming a best-case scenario that a low efficiency of $\epsilon_c \sim 10^{-22}$ cm^2 applies, we should expect that the deepest penetration is $N \sim \frac{1}{e \times 10^{-22}\,\mathrm{cm}^2} \sim 4 \times 10^{21}$ cm^{-2} and is achieved for an energy of ~ 700 eV. As we move towards the outer disc and ϵ_c increases, we should see this peak decrease and shift to lower energies.

Based on these results, we adopt a fiducial value of $\epsilon_c = 10^{-22}$ cm^2 and can then use equation (7) to calculate the maximum penetration depth as a function of energy. This is shown as the black dashed line in Fig. 4. We can see that this excellently captures the shape, normalization and maximum of the simulation curves. This validates our toy model and explains why the efficacy of wind driving is such a strong function of energy. In particular, it demonstrates why 1000 eV X-rays (employed by WG17) are too weakly interacting to heat material to $T_{\rm Bern}$, whereas energies of 500−700 eV are most potent. The fact that despite its simplicity, this model so well captures the dependence across a range of energies – which penetrate to depths with different densities and thus different associated cooling rates – suggests that it is largely the attenuation of radiation, and not the variation in cooling, that determines the base – this is in line with our earlier discussion of the assumption of optically thin heating being insufficient.

Note that this model also explains the small differences between the Full and IRFLNoH models. We see in Fig. 5 that the cooling rates only diverge as $T_{\rm Bern}$ becomes larger in the inner disc due to the reduced cooling of the IRFLNoH model which lowers ϵ_c (Fig. 5). This makes it easier to heat a larger column at small radii in the disc. Intermediate radii also see a somewhat increased potency for winds being driven by the harder frequencies (Fig. 4), but the largest radii with the coldest $T_{\rm Bern}$ are essentially unaffected.

4.3 Effect of luminosity

The spectrum of WG17 has relatively less X-ray compared to its UV flux (i.e. is overall softer) than that of (Ercolano et al. 2009); therefore, as well as the choice of the single X-ray band (the correct value of which will be determined by the shape of the X-ray spectrum), the relative luminosities could also be acting to diminish or enhance the role of X-ray between these studies. Fig. 6 therefore shows the column density to the Bernoulli surface for each energy for our X### simulations which have 6.25 times the X-ray luminosity of the S### simulations and which therefore reproduce the ratio of $L_X/L_{\rm EUV} = 0.8$ in the multifrequency input spectrum employed by Ercolano et al. (2009).

At the low-energy end, where the optical depths are high, this has relatively little effect on the columns reached. Greater difference is seen as we move to higher energies, where the column no longer peaks around 500−700 eV; indeed among those frequencies tested, 1000 eV was the most effective. This is in line with our explanatory model – since $\epsilon_c \propto 1/\xi \propto 1/L_X$, then the appropriate $\epsilon_c \sim 1.6 \times 10^{-23}$. With this lowered ϵ_c our model (black dashed line) remains an excellent fit and we would thus expect the highest column to be reached for X-ray energy of around 1350 eV in this case.

We note that the peak column $N \propto 1/\epsilon_c \propto L_X$. Therefore, since we have argued it is reasonable to assume that the column density in any wind scales with the mass-loss rate of the wind, then one would expect $\dot{M} \propto L_X$; this is roughly as observed in previous hydrodynamical simulations (Owen et al. 2012; Picogna et al. 2019) that found X-ray-driven wind solutions. Thus, by making more energy available in the X-ray, the ability of X-rays, in particular the harder bands, to drive a wind can be improved. Nevertheless, the choice of frequency still has a strong effect on the outcome. Since the X-ray luminosity is an inherently variable quantity (and closely tied to the stellar mass), the notion of the most effective energy for driving the wind will be linked to stellar properties.

Finally, we note that both the EUV luminosity and X-ray luminosity are likely to vary between stars. In models of EUV-driven winds under direct irradiation, the base densities (and wind densities) scale with the number of ionizing photons as $n_{\rm base} \propto \Phi^{1/2}$ (e.g. Hollenbach et al. 1994; Tanaka et al. 2013) which can be understood from a simple Strömgren-volume approach. The ϵ_c to be overcome in order for X-ray to heat below the EUV-heated base therefore also scales as $\Phi^{1/2}$; thus, we could get the same result as here by lowering the EUV luminosity by two orders of magnitude. Moreover if the X-ray luminosity scales more strongly than $\Phi^{1/2}$, then ϵ_c becomes a decreasing function of L_X and so higher luminosity sources will be more likely to host X-ray-driven winds, while sufficiently low L_X would lead to EUV-driven winds; these trends would be reversed if L_X is a relatively weak function of Φ.

4.4 Monochromatic versus full-spectrum modelling

A simplification in the above argument is that heating is assumed to be driven by only one frequency of radiation. In reality in these

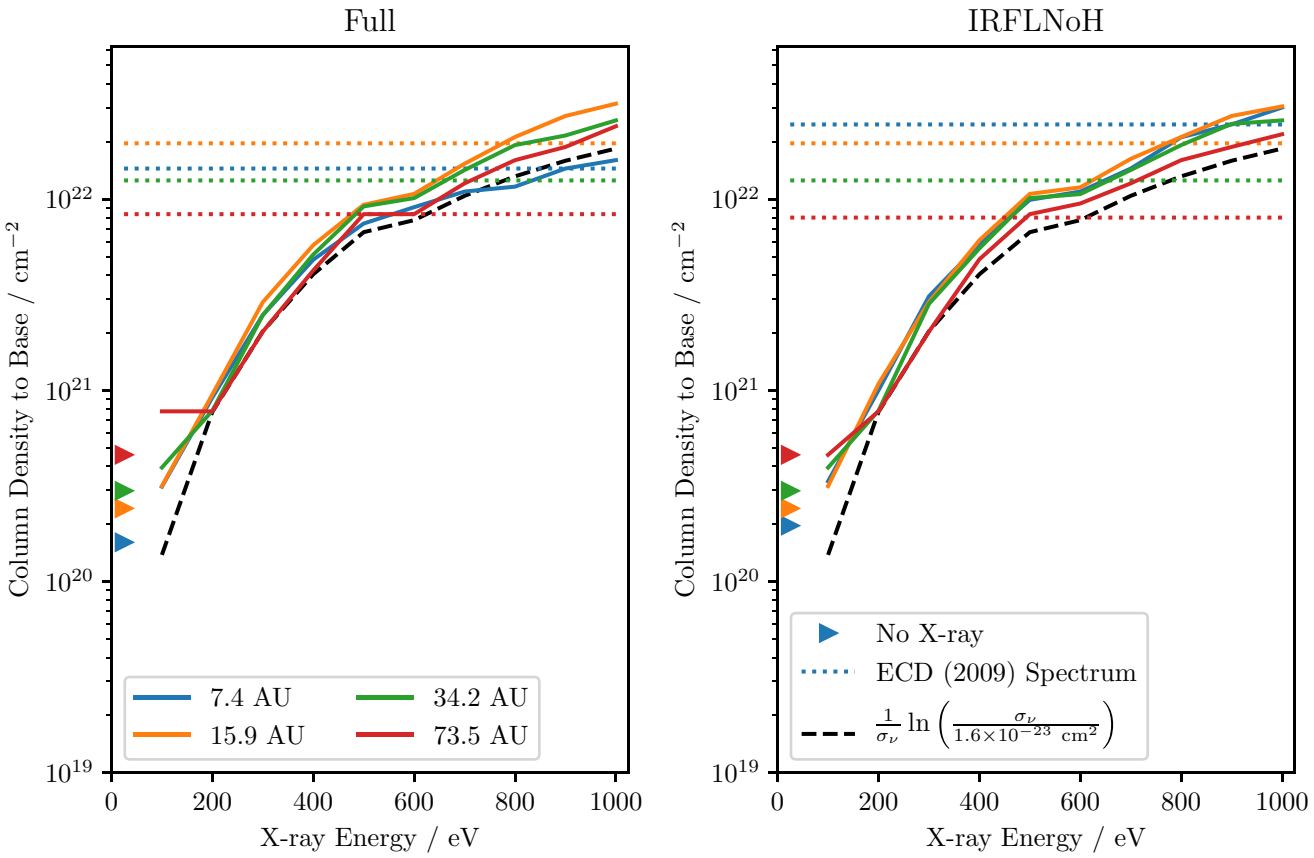

Figure 6. As Fig. 4 but for an increased X-ray luminosity $L_X = 1.6 \times 10^{31}$ erg s^{-1}. The coloured dotted lines are the values obtained using Ercolano et al. (2009)'s spectrum. The dashed line is equation (7) for $\epsilon_c = 1.6 \times 10^{-23}$ cm^2.

models, as aforementioned, FUV is assisting through photoionization of carbon and sulfur,[10] making it a little easier to launch a wind.

Moreover, a realistic X-ray spectrum would have a range of bins with different efficiencies – and with different individual luminosities and hence contributions to the spectrum – all working together: one might suppose that such a spectrum would be intermediate in terms of heated column compared with monochromatic models at a few hundred and 1000 eV since more energy is present in the effective bands than in the most extreme cases but it is not all concentrated there. We use the spectrum of Ercolano et al. (2009) as an illustrative example to explore this.

Fig. 6 shows, as dotted lines, the column achieved by Spectrum E at each radius. As predicted, the heated column is somewhat intermediate between that at low energies and 1000 eV. Spectrum E heats a substantially higher column than any of the monochromatic spectra in our S### series (see Fig. 4), mainly because of the roughly 10 fold higher total X-ray luminosity for models normalized to the same EUV flux. Thus, the overall shape of the spectrum of Ercolano et al. (2009), namely that it is harder than WG17's (and so when normalised to the same EUV flux has almost an order of magnitude higher X-ray luminosity) is a further key reason why it allows a somewhat deeper heating of a wind and leads to higher mass-loss rate, X-ray driven, models.

To quantify what we would expect for a continuous spectrum, we can attempt to generalise our model by replacing the single frequency treatment with an integral over frequency (cf. the attenuation factor of Krolik & Kallman 1983; Alexander et al. 2004b):

$$L_X \sigma_\nu \mathrm{e}^{-N\sigma_\nu} \rightarrow \int_{E>100\,\mathrm{eV}} \Phi_\nu \sigma_\nu \mathrm{e}^{-N\sigma_\nu} \mathrm{d}\nu \tag{8}$$

for the spectral flux Φ_ν. Thus, our modified condition for sufficient heating to launch a wind becomes

$$\epsilon_{\mathrm{eff}}(N) := \int_{E>100\,\mathrm{eV}} f_\nu \epsilon_\nu \mathrm{d}\nu \geq \epsilon_c, \tag{9}$$

where $f_\nu = \Phi_\nu / L_X$ and thus the effective efficiency $\epsilon_{\mathrm{eff}}(N)$ is a flux-weighted average efficiency. We can therefore iteratively calculate ϵ_{eff} for increasingly large N until it no longer satisfies the inequality in equation (9); the maximum N will be our estimate of the heated column.

The left-hand panel of Fig. 7 shows the column density estimated from this method at each radius plotted against the column density to the Bernoulli surface for the E_Full and E_IRFLNoH models. There is a good agreement between the model and the true densities for most points at $\gtrsim 10^{21}$ cm^{-2} and so we conclude that our model can be extended accurately to full spectra.

Clearly therefore, based on the arguments above, the most representative frequency is neither an ineffective one nor the most optimal one as much of the energy can be in less efficient bands. However, for a given combination of N and ϵ_{eff}, we can ask what single frequency would produce the same efficiency at that column. There are two solutions, the lower and high-energy ones having cross-sections $\sigma_1 = -\frac{1}{N} W_{-1}(-N\epsilon_{\mathrm{eff}})$ and $\sigma_2 = -\frac{1}{N} W_0(-N\epsilon_{\mathrm{eff}})$ where W_0

[10]While the dust is also FUV heated and is a significant source of opacity, it is a net coolant of the gas in these regions.

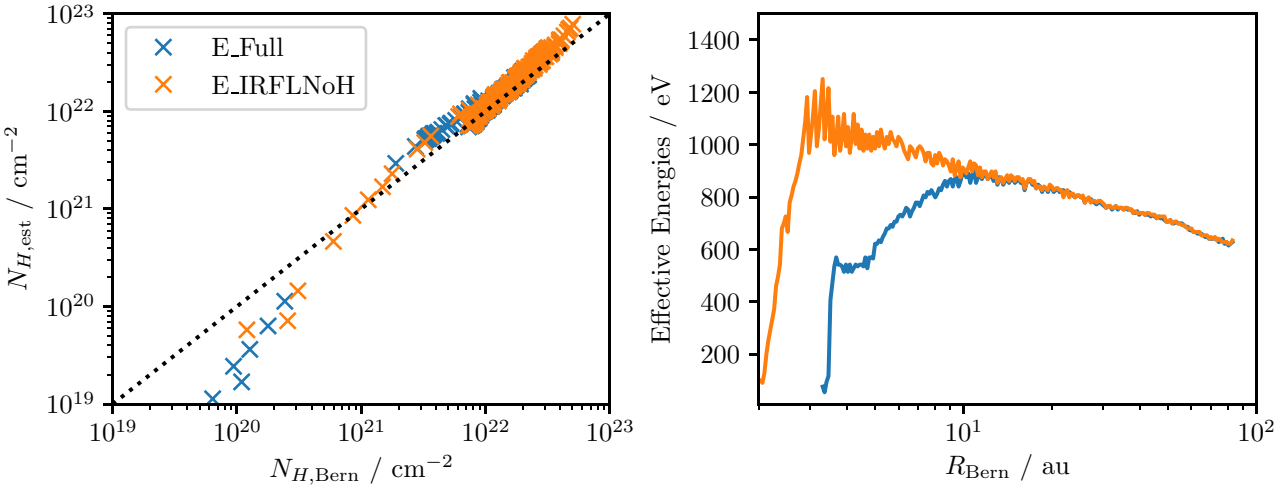

Figure 7. Left-hand panel: the column to the Bernoulli surface estimated from the cooling rates and spectrum using the toy model as a function of the true column to Bernoulli surface in the simulations with spectrum E – good agreement is seen especially at large columns. Right-hand panel: the lower of the two energies with heating efficiency equal to the effective efficiency of the whole spectrum at the relevant column as a function of radius.

and W_{-1} are the two real branches of the Lambert W function. For each radius in the simulations with spectrum E, the lower of these two energies is indicated on the right-hand panel of Fig. 7, while the higher energy solution is generally not realistic for X-ray spectra of low-mass stars and so is not depicted. As usual, very little difference is seen between the cooling models outside of ~ 10 au. We expect these energies to be a function of column as higher columns will progressively attenuate the spectrum at its harder end, meaning that what reaches the base will be better approximated by softer energies. Thus, as the column to the Bernoulli surface can vary with radius, the most representative energies also change, making it hard to reasonably pick a single frequency that would drive the wind everywhere with complete accuracy compared to a full spectrum. Nevertheless, for both cooling models, outside the innermost few au, the appropriate energies are always < 1000 eV, further suggesting that this choice by WG17 may not be an appropriate one. In the outer disc, the most representative energy is around 600 eV and would expected to drive an X-ray wind from the whole disc given the cooling rates assumed here.

More recent spectra as used by Ercolano et al. (2021) are somewhat softer than that used here, particularly for the lowest luminosity stars. These are therefore better represented by even softer energies from 400−800 eV for $L_X = 10^{31}$ erg s^{-1} to close to 100 eV for $L_X = 10^{29}-10^{30}$ erg s^{-1}. This may lead to less effective photoevaporation as these energies are less effective than ~ 600 eV due to their shallower penetration, though Ercolano et al. (2021) do still see a substantial X-ray-driven wind. Similarly, Nakatani et al. (2018b) used the TW Hya spectrum from Nomura et al. (2007) which is very soft due to its 'soft X-ray excess' (Güdel & Nazé 2009); its representative energies should therefore be very low, which may be a factor in their result that X-rays are ineffective drivers of photoevaporation on their own.

5 DISCUSSION: COOLING AND HEATING PROCESSES

We have so far explored how the ability of X-rays to heat the gas sufficiently depends on their frequency and shown that only those with energies of a few 100 eV can overcome the cooling included in our radiative transfer models. It is therefore important to consider more closely the impact of differences in how cooling is treated between photoevaporation models. To provide a baseline comparison, we first determine the dominant cooling channels in our models, before exploring the impact of the additional cooling channels discussed by WG17 as differences in methodology between their work and that of Owen et al. (2010): neutral sulfur, adiabatic cooling, and molecular cooling.

Fig. 8 shows three key cooling channels in our models – from left- to right-hand panels: collisionally exited Lyman lines of H, CELs of metals and recombinations – for the fiducial spectrum W. The top row indicates their fractional contribution to the cooling for the Full cooling and the bottom row for IRFLNoH.

For the Full cooling, the wind has fairly equal contributions to the cooling from Lyman radiation and metal CELs, with the former dominating slightly at larger radii and vice versa. Metal CELs are almost entirely responsible for cooling below the wind base, while recombinations play only a minor role in the wind and none below the base where the material is most neutral. For the IRFLNoH cooling, the Lyman lines have been switched off and play no part in the cooling. The metal CELs are still dominant below the base, but are heavily suppressed in the wind region as this contribution was largely down to optical lines, particularly those of S II. Instead, cooling in the wind is now almost entirely dominated by recombinations, which was the only significant non-adiabatic cooling in this region according to WG17.

This confirms that in the bulk of the wind, we expect significantly higher levels of non-adiabatic cooling than found by WG17 in the form of the Lyman lines and optical CELs. This is sufficient to explain the cooler wind temperatures seen for the Full cooling model and indeed in most photoevaporation models (e.g. Owen et al. 2012). The reason WG17 do not see significant Lyman cooling is because the optical depth of these lines is approximately $10^3 \lesssim \tau_{\mathrm{Ly}\alpha} \lesssim 10^5$ with escape probabilities $10^{-5} \rightarrow 10^{-4}$ meaning this cooling is several orders of magnitude weaker if the radiation is not allowed to escape through the line wings or as a result of absorption and re-radiation in the IR by dust.

On the other hand, at the temperatures around T_{Bern} and below the wind base, there is less difference between the cooling models. This region is well described as a PDR – which are typically cooled

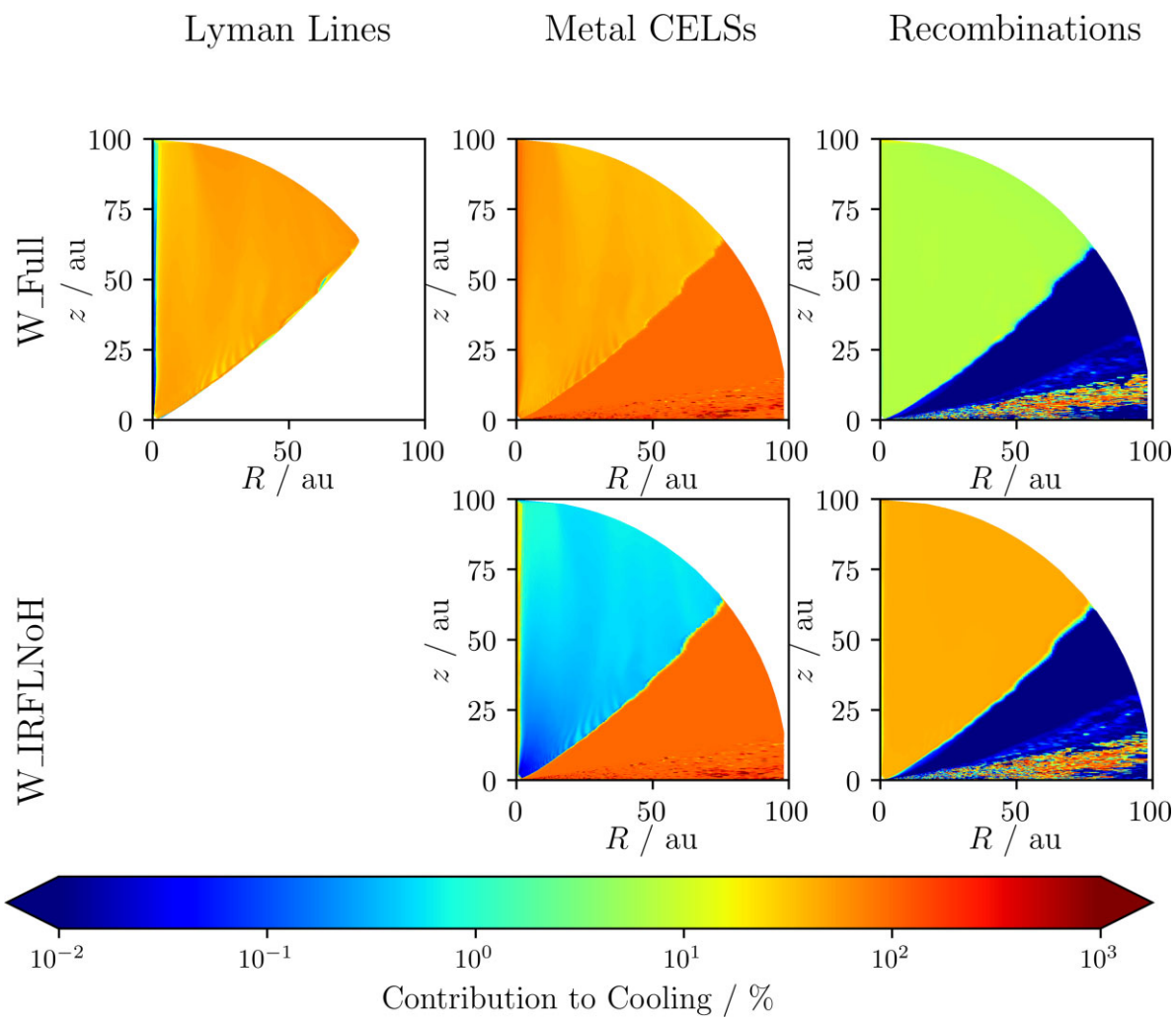

Figure 8. The percentage contribution to the cooling from three key processes: permitted line Lyman radiation from collisionally excited H, forbidden line radiation from collisionally excited metals, and recombinations in the fiducial simulations. The top row shows the Full cooling model where cooling is dominated by Lyman lines and metal CELs. The bottom row shows the IRFLNoH model – here Lyman lines are switched off and the Metal CELs severely suppressed, increasing the role of recombinations in the wind region. Note that percentages greater than 100 are recorded near the mid-plane as MOCASSIN treats dust as a coolant but here it can become warmer than the gas and has a net heating effect, i.e. a negative cooling contribution.

mainly by [O I] 63 and [C II] 158 μm (Tielens & Hollenbach 1985) – and so the set of coolants considered by WG17 is appropriate here.

5.1 Sulfur

Unlike previous works applying MOCASSIN, our models include neutral sulfur. Within the wind itself, sulfur is mostly doubly ionized, with a non-negligible contribution from singly ionized sulfur but little neutral sulfur remaining. On the other hand, below the base sulfur is mostly singly ionized by FUV in the heated region, transitioning to mostly neutral beyond this. The inclusion of neutral sulfur will therefore make negligible difference to the temperatures of the wind itself, while having the most impact wherever the disc becomes optically thin to FUV; the X-rays most efficient at heating this region and thus those most affected will be those with similar cross-sections to FUV, i.e. with energies $\gtrsim 1$ keV. However, since our results show that X-rays (including the hard 1 keV X-rays for some radii) are able to heat material to escape even with the inclusion of neutral sulfur, we must conclude that it is not a critical cause for the differences seen between WG17 and Owen et al. (2010). On the other hand, there are optical CELs of S II that are significant coolants and are not included by WG17, which is one contributing factor to their hot wind temperatures.

5.2 Hydrodynamical cooling

The main difference that WG17 claim in the wind region is that adiabatic expansion overwhelmingly dominates the cooling and offsets the photoionization heating. We have already seen how the inclusion of optical forbidden lines and unattenuated Lyman lines can increase the non-adiabatic cooling budget significantly, making it more competitive with the adiabatic contribution. Before quantifying how much so, it is useful to discuss what is meant by adiabatic cooling.

The evolution of the total energy density $E = \rho\epsilon = \frac{1}{2}\rho v^2 + \rho u + \rho\Phi$ in a static potential Φ is described by the energy equation

$$\frac{\partial E}{\partial t} + \nabla \cdot ((E + P)\vec{v}) = \rho(\Gamma - \Lambda), \tag{10}$$

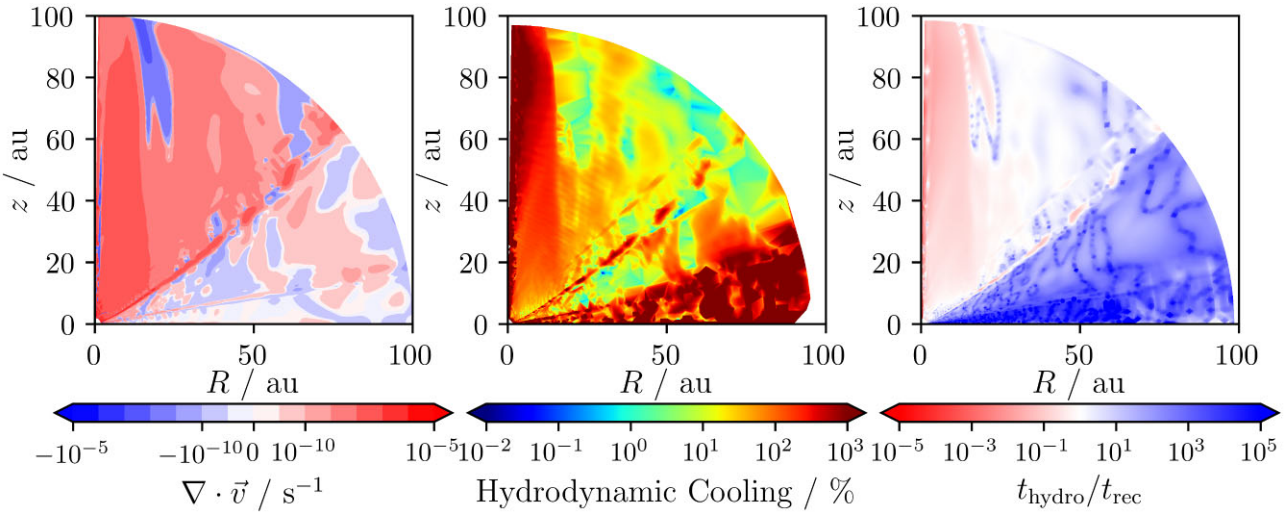

Figure 9. Estimates of the significance of hydrodynamical cooling for simulation W_Full. The leftmost panel shows the divergence of the velocity grid from WG17 with diverging flows in red and converging flows in blue. The central panel shows the hydrodynamical cooling relative to the total MOCASSIN cooling expressed as a percentage. The large values near the mid-plane are likely an artefact of the low cooling rates there. The rightmost panel shows an estimate of the ratio between the hydrodynamic and cooling (recombination) time-scales with red regions indicating shorter hydrodynamic time-scales and blue indicating regions where the radiative equilibrium is reasonable to assume.

for heating and cooling rates per unit mass Γ and Λ, respectively. The corresponding equation (in conservative form) for the thermal energy density ρu is

$$\frac{\partial}{\partial t}(\rho u) + \nabla \cdot (\rho u \vec{v}) = \rho \frac{Du}{Dt} = \rho(\Gamma - \Lambda) - P \nabla \cdot \vec{v}. \quad (11)$$

The additional term, on the right-hand side, compared to equation (10) represents the 'PdV' work done on fluid element by expansion in the presence of a diverging velocity field which adiabatically cools the gas. The energy lost from the thermal contribution is used to accelerate the wind by pressure gradients along the streamlines.

However, in establishing a steady state thermal balance, we are more interested in the thermal evolution at a particular location:

$$\frac{\partial u}{\partial t} = (\Gamma - \Lambda) - (\gamma - 1) u \nabla \cdot \vec{v} - \vec{v} \cdot \nabla u. \quad (12)$$

Thus, while adiabatic cooling is relevant for the cooling of a fluid element, the advection of thermal energy also plays an important role when setting the thermal balance in an Eulerian sense. This thermal flux could potentially offset the adiabatic cooling if material flows from hot to cold and should also be considered.

In steady state, integrating equation (10) over a volume following a streamline bundle and using mass conservation gives

$$\dot{M} \Delta \epsilon_{\rm tot} = L_{\rm heat} - L_{\rm cool}, \quad (13)$$

where $\Delta \epsilon_{\rm tot}$ is the difference between the mass-flux-weighted average energy density at either end of the bundle. Owen et al. (2010) argue that since $\dot{M} \Delta \epsilon_{\rm tot} \lesssim 8\% L_X$, then the advected energy is negligible compared to $L_{\rm heat}$ can assume $L_{\rm heat} \approx L_{\rm cool}$. This relies on the assumption that $L_{\rm heat} \approx L_X$, which may not be true if significant luminosities lie at harder energies that penetrate through the wind base and are absorbed at longer columns. While this result has not been thoroughly investigated for a range of luminosities, since $\dot{M}$ is typically found to scale approximately linearly with L_X (Owen et al. 2011; Picogna et al. 2019) – except at the highest luminosities – then the argument should translate. Moreover, in all the spectra here, $L_{\rm heat} \gtrsim L_{\rm EUV} \gtrsim L_X$ so in any case this would not affect the conclusion strongly.

Moreover, integrating for the thermal energy density u,

$$\dot{M} \Delta u_{\rm tot} = L_{\rm heat} - L_{\rm cool} - L_{\rm adiabatic}. \quad (14)$$

Hence, by comparison we conclude that $\dot{M} \Delta \epsilon_{\rm tot} = \dot{M} \Delta u_{\rm tot} + L_{\rm adiabatic}$ and the advected energy is the net result of any advected thermal energy less any adiabatic cooling. Since the wind consists of unbound material, and is being accelerated, it is reasonable to assume the dominant contribution to the advected energy is an increase in kinetic energy – since the wind ends up supersonic, this is likely of greater magnitude than any change in thermal energy i.e. $\dot{M} \Delta \epsilon_{\rm tot} >> \dot{M} \Delta u_{\rm tot}$ and hence $L_{\rm adiabatic} \approx \dot{M} \Delta \epsilon_{\rm tot}$ and probably should not be significantly offset by thermal advection.

Fig. 9 shows quantities relevant to hydrodynamical cooling for the W_Full simulation. First, the left-most panel shows the divergence of the velocity field $\nabla \cdot \vec{v}$ from WG17 (since we do not recalculate this for our temperature field). Indeed, over most of the wind volume, the velocity field is diverging which would result in cooling of the material. It can be seen that this is particularly strong in a column at $R \lesssim 20$ au – this is a result of a strong acceleration in the radial direction.

The net hydrodynamical cooling as a percentage of the non-adiabatic calculation from MOCASSIN (using the temperatures and cooling rates of the W_Full simulation) is shown in the middle panel of Fig. 9. We can see that correspondingly, while in most of the volume, it can only account for around 10 per cent of the cooling (i.e. similar to the value found by Owen et al. 2010, for material originating at $R \approx 20$ au) – making it a not insignificant (compared to e.g. recombinations) but nevertheless non-dominant contribution – adiabatic cooling is important at $R \lesssim 20$ au.[11] This suggests that the cooler temperatures seen by WG17 in this region than in our W_IRFLNoH simulation are a result of additional adiabatic cooling, which is strongest – at least for a mild temperature gradient – at small radii. There are also a few hotspots where adiabatic cooling may be

[11] While included in the calculation, thermal advection is negligible here as the wind region is close to isothermal.

important near the base of the wind as the material is accelerated through the wind base suggesting adiabatic cooling may have some effect on the launching of the wind.

As a further check, in the right-hand hand panel, we show the ratio of the hydrodynamical time-scale (estimated as $|\nabla \cdot \vec{v}|^{-1}$) and the recombination time-scale [$1.5 \times 10^9 T_e^{0.8} n_e^{-1}$, which is usually the longest microphysical time-scale Ferland (1979), Salz et al. (2015)]. Again, we see that in the bulk of the wind and base the hydrodynamical time-scale is around an order of magnitude longer and we can safely assume radiative thermal equilibrium but that near the z-axis the hydrodynamical time-scale is shorter and the assumption may break down.

It is notable that the estimates of time-scales are much more comparable than were found by Picogna et al. (2019). On the one hand, the temperatures are a little higher here which increases the typical velocity scale ($c_S \propto T^{0.5}$) and hence decreases the hydrodynamical time-scale, while the recombination time-scale increases as the electrons are more energetic and harder to recapture. Moreover, the hydrodynamical time-scale is independent of density, while the time-scales of two-body non-adiabatic cooling processes are longer at the low densities of the EUV-driven density profile of WG17 compared to the higher densities in Picogna et al.'s (2019) X-ray-driven wind (although lower X-ray luminosities may drive somewhat less dense winds in which this time-scale is not so long and hence radiative equilibrium a less robust assumption).

We conclude that the contribution from adiabatic cooling shown in Fig. 9 probably represents an upper bound; this contribution should be less significant in the cooler, denser X-ray-driven winds which we argue should result from the use of a softer X-ray spectrum than that employed by WG17. Nevertheless, adiabatic cooling should probably be considered further across the X-ray luminosity range, particularly when modelling the inner wind regions and their tracers (e.g. [O I] 6300 Å Ercolano & Owen 2016).

5.3 Molecules

Molecules, likely to be present in the underlying disc, are the final missing piece of our model compared to that of WG17 or Nakatani et al. (2018b). We thus conclude our exploration of the different cooling contributions by considering the potential consequences of including molecules on ability of X-rays to launch a wind and the resultant wind mass-loss rates.

In Section 3, we showed that irradiating WG17's density grids using MOCASSIN produced warmer temperatures below the IF and in Section 4 that this persisted once X-rays were removed entirely. This implies extra cooling is needed below the base to fully reproduce WG17: since sulfur is included in our models and adiabatic cooling is relatively negligible in this region the best candidate is molecular cooling: rovibrational lines of molecular species (partiularly H_2, H_2O, OH) can be the dominant radiative processes just below the base (WG17).

By increasing the available cooling at temperatures $\sim T_{\rm Bern}$, further cooling from molecules would affect the quantitative results of Section 4.2 as to both (a) which X-rays can launch a wind and (b) which are most effective at doing so. These mechanisms could be particularly significant in the cooler outer disc or at high optical depths to FUV, where molecular survival is more likely. However, even at small/intermediate radii, extra cooling should reduce the ability of 1000 eV X-ray to drive a wind somewhat (cf the Full models versus the IRFLNoH models) potentially even to the extent of eliminating X-ray-driven winds entirely (as seen by WG17).

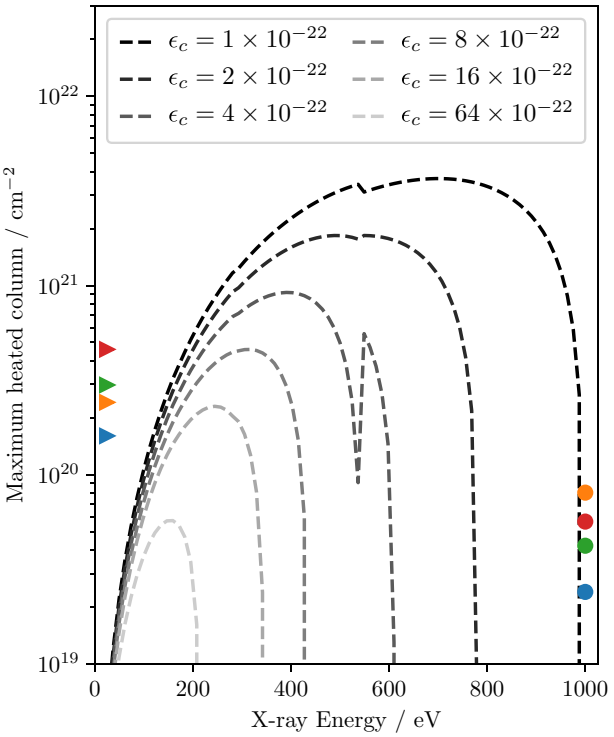

Figure 10. Effect of additional cooling on the maximum column that can be heated to $T_{\rm Bern}$. Additional cooling is parametrized as an increase in ϵ_c and represented by increasingly light colours. The kinks in some curves are because of a non-monotonicity in the photoionization cross-section due to inner shell ionization of oxygen. The coloured triangles represent the column reached in our UV-only model for the same range of radii as in Fig. 4.

Properly quantifying the contribution of molecules is beyond the scope of this work, but since the additional cooling would increase ϵ_c (equation 6), then we can start by considering the impact of some representative increases in this parameter on the column which each X-ray frequency can heat (equation 7) and which frequency is optimal for launching a wind.

Fig. 10 shows that the curve of maximum heated column versus energy shifts down to lower columns (and to the left, peaking at lower energies) as ϵ_c is increased. An increase by a factor $\sim$8 would be needed to prevent any X-ray from being able to heat a higher column than our UV-only simulations to $T_{\rm Bern}$ at large radii, and an increase by $\gtrsim 16$ would be needed to achieve this at all radii. Moreover, in this limit, only very soft X-rays 200−400 would have any significant heating effect. However, this is likely an underestimate of the necessary cooling since the column heated in these reference simulations would likely also be reduced somewhat towards the values found by WG17. An increase in ϵ_c of more like 30−100 × may therefore be required to prevent any single X-ray from heating the wind.

Therefore to significantly affect our conclusion about the viability of X-ray wind launching at softer energies, molecules – or any other additional cooling not included in MOCASSIN – would need to contribute at least an order of magnitude more cooling than the atomic processes here modelled. It is worth noting however, that such an increase in ϵ_c could also be caused by a decrease in the X-ray luminosity available to heat the wind, or the efficiency with which X-rays are able to deposit the absorbed energy into the gas due to losses to secondary ionization by the photoelectrons before they thermalize

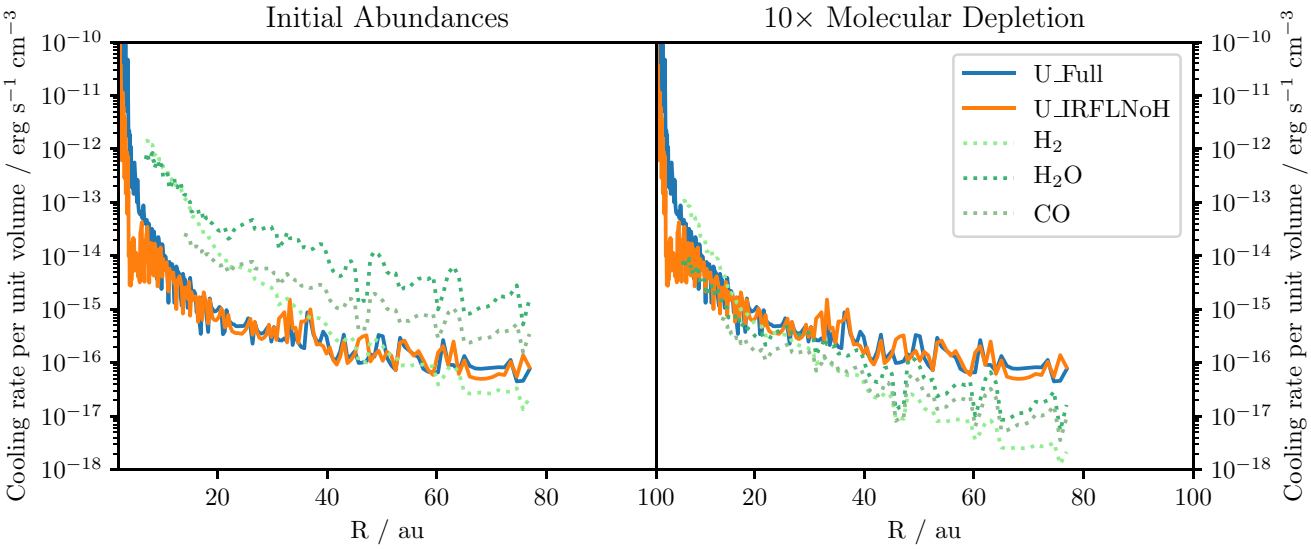

Figure 11. Cooling rates per unit volume for the U_Full (blue) and U_IRFLNoH (orange) simulations at the Bernoulli surface. The dotted lines show the possible contribution of additional molecular cooling from H_2, H_2O, and CO, on the left-hand panel with maximal abundances assuming all atoms are in molecules and on the right-hand panel with molecular abundances depleted by 10 times from the maximal values.

(see Section 5.4). Conversely, increases in these parameters would make it harder for molecular cooling to prevent an X-ray heated wind.

To estimate whether molecules have this potential, we provide estimates for the impact of molecular ro-vibrational cooling along the Bernoulli surface from the U_IRFLNoH model using the tabulations for H_2, H_2O, and CO from Neufeld & Kaufman (1993). We choose to match the initial molecular abundances of WG17 and in each case, we assume that the wind base is optically thin and so set the optical depth parameter to its minimal tabulated value. The calculated cooling rates are shown alongside those from the U_Full and U_IRFLNoH simulations on the left-hand panel of Fig. 11. The most significant cooling typically comes from water, which under these assumptions can contribute more than an order of magnitude more cooling than the atomic processes thus suggesting a potentially important role for molecular cooling in the framework set out above.

However, there are two important caveats: first, that we ignore any possible molecular heating. For example, FUV pumping into the Lyman and Werner bands followed by collisional de-excitation from the vibrationally excited states of the ground electronic state can result in net heating of gas by H_2. Secondly, in following WG17's inital molecular abundances we have made the most generous assumption that all C, O, and H will be in molecules. In reality molecular abundances are likely to be somewhat lower than this at the base: since FUV is generally more penetrating than EUV or soft X-rays, the base will be optically thin to FUV which will lead to molecular dissociation. Moreover, the warm upper layers of protoplanetary discs are frequently observed to be depleted in volatile molecules such as H_2O by a couple of orders of magnitude (e.g. Du et al. 2017) due to freeze-out on to ice grains that settle to the mid-plane (though such processes would also affect atomic coolants). The right-hand panel of 11 demonstrates that an order of magnitude depletion in all molecular abundances near the base would be sufficient to make them subdominant coolants to atoms.

A further caveat is that we have only considered molecular effects in the context of a single X-ray frequency. As discussed in Section 4.4, when a full spectrum is considered the heated column is somewhat less than for the most efficient frequencies. Our estimate that an order-of-magnitude more cooling may be needed to prevent an X-ray wind may therefore be a slight overestimate and molecules may not need to prevent all X-ray energies from heating the wind. However, a moderate increase of around a factor of 4 can likely still be tolerated, since in Section 4.4 we showed that $\sim 600\,\mathrm{eV}$ would be representative of the integrated spectrum and effective heating at $\gtrsim 600\,\mathrm{eV}$ is prevented for a factor of $\gtrsim 4$ increase in cooling. Other spectra used in the recent literature (Nomura et al. 2007; Ercolano et al. 2021) are softer than those used here so the representative energies are in regions that are more robust against being rendered ineffective by additional cooling since they lie in the attenuation-limited (optically thick) regime (whereas additional cooling progressively limits the effect of harder energies). However, as aforementioned, the effects of additional cooling and the X-ray luminosity are degenerate, so since the hardest spectra tend to be found for stars with the highest L_X, the X-ray heating for harder spectra has a 'head start' against the effects of additional molecular cooling.

Our simulations show hotter temperatures below the base. The thermal structure here is also important to determining the mass-loss rates as it determines hydrostatic equilibrium. For example, with only the cooling present in our simulations, one would therefore expect to see the disc region puff up more, which can result in the disc intercepting more of the driving radiation, assisting mass-loss rates (WG17). Furthermore, the momentum flux (and hence mass-loss rate) of the wind depends on the pressure jump across the base, which depends on the temperature to which the underlying material is heated.

Thus, as an upper bound, molecules certainly would lead to X-rays being able to unbind gas less dense gas (at lower columns) than otherwise and thus decrease mass-loss rates. Moreover, without molecules we likely overestimate the temperature/pressure on the underside of the disc somewhat affecting its hydrostatic structure and momentum flux, which would lead to an overestimate of mass-loss rates if we tried to infer them from our models. This is all consistent with the fact that WG17's fiducial model has a lower mass-loss rate

than their OECA10 analog which did not include molecular cooling. Moreover, like WG17 and Nakatani et al. (2018b), who also included molecules, found that X-rays were not able to drive a wind, despite their softer spectrum that peaks at a few 100 eV. However, they do not include cooling from water, which seems to be the most significant molecular coolant if abundant.

Altogether it is unclear whether, other than in the most generous scenario, molecular cooling could reduce the role of X-ray enough to result in an EUV-driven wind. A self-consistent calculation of molecular abundances with a realistic X-ray spectrum is needed to more accurately determine their role in competing against X-ray heating.

5.4 X-ray heating fraction

In applying our explanatory model, we have set $f_X = 1$ as is appropriate for a UV-heated wind. As aforementioned, the true value may be lower, which is likely the case at the base of an X-ray-driven wind since X-ray heated material has low levels of ionization. Given the degeneracy noted earlier, the effect of such a lower f_X can be understood in exactly the same terms as any additional cooling, by using Fig. 10. That fact that the explanatory model with $f_X = 1$ still fits the data well however, suggests this does not have a large effect on our results.

We note that Nakatani et al. (2018b) (and also e.g. Gorti & Hollenbach 2004) use treat the X-ray heating by simply assuming f_X to lie in the range 10−40 per cent depending on the relative fractions of atomic and molecular gas, regardless of levels of ionization. By comparison to Fig. 10, we may expect this could have a significant effect on the ability of X-rays to heat a wind and may contribute (alongside their inclusion of molecular cooling, their very low X-ray to EUV luminosity ratio, and their X-ray spectrum dominated by a very soft excess) to the fact that they do not see a significant direct role for X-ray in launching a wind (note that conversely when they assume 100 per cent of the photoelectron energy thermalizes they do indeed find a more significant role for X-rays).

6 CONCLUSIONS

We have explored the ability of different bands of radiation to drive a thermal wind by irradiating the density grid of WG17 using MOCASSIN in order to probe potential systematic differences between models of photoevaporative winds. Such systematic differences include the fundamental approach to radiative transfer, the cooling processes included and the nature of the irradiating spectrum We have further used a simple toy model of thermal equilibrium to rationalize the results of these experiments. Here, we set out the key findings before summarizing what it will take to accurately determine photoevaporative mass-loss rates.

(i) The ability of X-rays to heat a higher column than the EUV and hence launch an X-ray-driven wind is a strong function of frequency, which results from balancing the attenuation of lower frequencies against the larger column over which higher frequencies dissipate their energy. The most effective band – if one assumes the spectrum is effectively a delta function with a single frequency present – is ~ 500 eV for typical cooling rates and luminosities; changing the representative frequency to such a value would result in an X-ray driven – rather than EUV driven – wind with mass-loss rates a few times higher. In total, 1000 eV X-rays as used by WG17 are mostly unable to drive a wind (though may be marginally able to do so from restricted radii).

(ii) Moreover, a realistic spectrum contains a range of X-ray energies each contributing to heating according to the shape of the spectrum. While the most representative band changes as a function of column density and radius, making it difficult to pick any single value to use for an X-ray bin even for a given spectrum, 1000 eV is not a very representative energy anywhere or for any of the spectra considered.

(iii) The relative ability of different X-ray energies to drive a wind is also dependent on the luminosity with higher X-ray luminosities resulting in harder energies becoming effective (at fixed EUV luminosity).

(iv) Optical forbidden line radiation and Lyman α cooling mostly operate at higher temperatures than those at which material typically becomes unbound, so make relatively small differences to thermal balance where the wind is launched. Hence, our results are relatively insensitive to the treatment of these cooling mechanisms which varies between previous works.

(v) However, the high $\sim 3 \times 10^4$ K temperatures found in the wind of WG17 are a result of missing cooling in their work, namely the complete absence of optical forbidden line radiation and the treatment of Lyman radiation as optically thick and non-escaping.

(vi) Adiabatic cooling is a modest contributor to thermal balance over most of the grid compared to emission-line radiation once all such sources are accounted for. It may be most significant in regions of high acceleration such as in the low-density column near the z-axis. However, its significance would likely be lower in a cooler, denser X-ray heated wind at least for the $> 10^{30}$ erg s^{-1} luminosities considered here.

(vii) Molecular cooling can be relevant near the temperatures at which material becomes unbound. This manifests in our simulations, which lack molecular cooling, as hotter temperatures below the base than found in WG17. If generous assumptions are made about molecular abundances, molecular cooling – particularly from water – could play an important role in reducing the maximum column heated by X-rays and further preventing hard frequencies from having sufficient heating effect to launch a wind. However, it is likely somewhat more challenging for it to completely invert our conclusion that winds should be X-ray driven.

With all this is mind, we argue that it is crucial for modelling of thermal winds to play close attention to the choice of irradiating spectrum. If too hard (or too soft) an X-ray band is used, its ability to heat a column of material exceeding that heated by the EUV is diminished and an EUV-driven wind will result. Whereas, intermediate X-ray frequencies of a few 100 eV – as are, realistically, present in the ionizing spectra of T Tauri stars – should be able to launch an X-ray-driven wind. This is likely a key origin of conflicts between the X-ray driven photoevaporation models (e.g. Owen et al. 2012; Picogna et al. 2019) and EUV-driven models (WG17). However, a more appropriate choice of monochromatic frequency whose effect is equivalent to that of a realistic multifrequency spectrum is hard to define as it varies with columnm, radius and X-ray luminosity; moreover, the spectral shape can change as a function of stellar X-ray luminosity (Preibisch et al. 2005; Ercolano et al. 2021). Thus, it is not possible to capture the complete behaviour of X-ray heated winds too well with a single X-ray frequency.

Furthermore, the ability of radiation to launch a wind, particularly where harder frequencies are concerned, is dependent on the ability of photoionization heating to overcome the local cooling. Thus, accurately establishing a complete set of cooling processes and coolant abundances relevant to conditions at the wind base will prove key to determining the exact range of frequencies which are able to

overcome this and contribute to an X-ray-driven wind. Since X-ray-driven models so far (Owen et al. 2010, 2011, 2012; Picogna et al. 2019, 2021; Ercolano et al. 2021) all neglect some sources of cooling, it is likely that the true mass-loss rates are somewhat lower than derived from those works but may be less pessimistic than EUV-driven models would suggest.

Finally, we note that mass-loss rates would be expected to scale with the X-ray luminosity (Owen et al. 2012; Picogna et al. 2019) (which usually scales with stellar mass). In this work we have highlighted the importance of softer X-ray < 1000 eV and so the relevant X-ray luminosity is that emitted across the most effective frequencies. These luminosities are around a factor of 2 lower than the typically quoted values (which cover the 500−5000 ev range); such effects should be born in mind when choosing X-ray luminosities for disc evolution modelling – as has been explored further by Ercolano et al. (2021) – and recognizing the correct scaling of these properties with stellar properties should prove crucial to population synthesis.

ACKNOWLEDGEMENTS

We are grateful to Lile Wang for sharing the density grids used to conduct our simulations. We thank the anonymous reviewer for a careful reading and constructive suggestions that helped strengthen our arguments, as well as Richard Booth, and James Owen's group, for useful discussions on this work. ADS thanks the Science and Technology Facilities Council (STFC) for a PhD studentship and CJC acknowledges support from the STFC consolidated grant ST/S000623/1. This work has also been supported by the European Union's Horizon 2020 research and innovation programme under the Marie Sklodowska-Curie grant agreement No 823823 (DUST-BUSTERS). BE was supported by the Deutsche Forschungsgemeinschaft (DFG, German Research Foundation) Research Unit 'Transition discs' (FOR 2634/2, ER 685/8-2) and the Excellence Cluster ORIGINS of the German Research Foundation under Germany's Excellence Strategy – EXC-2094 – 390783311. This work was performed using resources provided by the Cambridge Service for Data Driven Discovery (CSD3) operated by the University of Cambridge Research Computing Service (www.csd3.cam.ac.uk), provided by Dell EMC and Intel using Tier-2 funding from the Engineering and Physical Sciences Research Council (capital grant EP/P020259/1), and DiRAC funding from the Science and Technology Facilities Council (www.dirac.ac.uk)

DATA AVAILABILITY

X-ray enabled MOCASSIN is available from https://github.com/rwesson/mocassin_xray. Temperature grids may be shared on reasonable request to the lead author.

REFERENCES

Alexander R., Pascucci I., Andrews S., Armitage P., Cieza L., 2014, in Beuther H., Klessen R. S., Dullemond C. P., Henning T., eds, Protostars and Planets VI. Univ. Arizona Press, Tucson, p.475
Alexander R. D., Clarke C. J., Pringle J. E., 2004a, MNRAS, 348, 879
Alexander R. D., Clarke C. J., Pringle J. E., 2004b, MNRAS, 354, 71
Alexander R. D., Clarke C. J., Pringle J. E., 2005, MNRAS, 358, 283
Avery L. W., House L. L., 1968, ApJ, 152, 493
Ballabio G., Alexander R. D., Clarke C. J., 2020, MNRAS, 496, 2932
Banzatti A., Pascucci I., Edwards S., Fang M., Gorti U., Flock M., 2019, ApJ, 870, 76
Clarke C. J., Alexander R. D., 2016, MNRAS, 460, 3044
Clarke C. J., Gendrin A., Sotomayor M., 2001, MNRAS, 328, 485
Cohen M., Harrington J. P., Hess R., 1984, ApJ, 283, 687
D'Alessio P., Calvet N., Hartmann L., 2001, ApJ, 553, 321
Dere K. P., Landi E., Mason H. E., Monsignori Fossi B. C., Young P. R., 1997, A&AS, 125, 149
Dere K. P., Del Zanna G., Young P. R., Landi E., Sutherland R. S., 2019, ApJS, 241, 22
Dijkstra M., 2017, preprint (arXiv:1704.03416)
Du F. et al., 2017, ApJ, 842, 98
Ercolano B., Owen J. E., 2010, MNRAS, 406, 1553
Ercolano B., Owen J. E., 2016, MNRAS, 460, 3472
Ercolano B., Pascucci I., 2017, R. Soc. Open Sci., 4, 170114
Ercolano B., Barlow M. J., Storey P. J., Liu X. W., 2003, MNRAS, 340, 1136
Ercolano B., Barlow M. J., Storey P. J., 2005, MNRAS, 362, 1038
Ercolano B., Young P. R., Drake J. J., Raymond J. C., 2008, ApJS, 175, 534
Ercolano B., Clarke C. J., Drake J. J., 2009, ApJ, 699, 1639
Ercolano B., Mayr D., Owen J. E., Rosotti G., Manara C. F., 2014, MNRAS, 439, 256
Ercolano B., Picogna G., Monsch K., Drake J. J., Preibisch T., 2021, MNRAS, 508, 1675
Fang M. et al., 2018, ApJ, 868, 28
Ferland G. J., 1979, MNRAS, 188, 669
Flaischlen S., Preibisch T., Manara C. F., Ercolano B., 2021, A&A, 648, A121
Font A. S., McCarthy I. G., Johnstone D., Ballantyne D. R., 2004, ApJ, 607, 890
Gahm G. F., Fredga K., Liseau R., Dravins D., 1979, A&A, 73, L4
Gorti U., Hollenbach D., 2004, ApJ, 613, 424
Gorti U., Hollenbach D., 2008, ApJ, 683, 287
Gorti U., Hollenbach D., 2009, ApJ, 690, 1539
Güdel M. et al., 2007, A&A, 468, 353
Güdel M., Nazé Y., 2009, A&A Rev., 17, 309
Hartigan P., Edwards S., Ghandour L., 1995, ApJ, 452, 736
Hartmann L., Calvet N., Gullbring E., D'Alessio P., 1998, ApJ, 495, 385
Hollenbach D., 2017, Mem. Soc. Astron. Italiana, 88, 685
Hollenbach D., McKee C. F., 1979, ApJS, 41, 555
Hollenbach D., Johnstone D., Lizano S., Shu F., 1994, ApJ, 428, 654
Koepferl C. M., Ercolano B., Dale J., Teixeira P. S., Ratzka T., Spezzi L., 2013, MNRAS, 428, 3327
Komaki A., Nakatani R., Yoshida N., 2021, ApJ, 910, 51
Krolik J. H., Kallman T. R., 1983, ApJ, 267, 610
Kunitomo M., Suzuki T. K., Inutsuka S.-I., 2020, MNRAS, 492, 3849
Kwan J., Krolik J. H., 1981, ApJ, 250, 478
Landi E., Del Zanna G., Young P. R., Dere K. P., Mason H. E., Landini M., 2006, ApJS, 162, 261
Liffman K., 2003, PASA, 20, 337
Maloney P. R., Hollenbach D. J., Tielens A. G. G. M., 1996, ApJ, 466, 561
Nakatani R., Hosokawa T., Yoshida N., Nomura H., Kuiper R., 2018a, ApJ, 857, 57
Nakatani R., Hosokawa T., Yoshida N., Nomura H., Kuiper R., 2018b, ApJ, 865, 75
Neufeld D. A., Kaufman M. J., 1993, ApJ, 418, 263
Nomura H., Aikawa Y., Tsujimoto M., Nakagawa Y., Millar T. J., 2007, ApJ, 661, 334
Owen J. E., Ercolano B., Clarke C. J., Alexander R. D., 2010, MNRAS, 401, 1415
Owen J. E., Ercolano B., Clarke C. J., 2011, MNRAS, 412, 13
Owen J. E., Clarke C. J., Ercolano B., 2012, MNRAS, 422, 1880
Picogna G., Ercolano B., Owen J. E., Weber M. L., 2019, MNRAS, 487, 691
Picogna G., Ercolano B., Espaillat C. C., 2021, MNRAS, 508, 3611
Preibisch T. et al., 2005, ApJS, 160, 401
Salz M., Banerjee R., Mignone A., Schneider P. C., Czesla S., Schmitt J. H. M. M., 2015, A&A, 576, A21
Sellek A. D., Booth R. A., Clarke C. J., 2020, MNRAS, 498, 2845
Sellek A. D., Clarke C. J., Booth R. A., 2021, MNRAS, 506, 1
Shull J. M., van Steenberg M. E., 1985, ApJ, 298, 268
Shu F. H., Johnstone D., Hollenbach D., 1993, Icarus, 106, 92
Simon M. N., Pascucci I., Edwards S., Feng W., Gorti U., Hollenbach D., Rigliaco E., Keane J. T., 2016, ApJ, 831, 169

Somigliana A., Toci C., Lodato G., Rosotti G., Manara C. F., 2020, MNRAS, 492, 1120
Tanaka K. E. I., Nakamoto T., Omukai K., 2013, ApJ, 773, 155
Tarter C. B., Tucker W. H., Salpeter E. E., 1969, ApJ, 156, 943
Tielens A. G. G. M., Hollenbach D., 1985, ApJ, 291, 722
Verner D. A., Yakovlev D. G., 1995, A&AS, 109, 125
Verner D. A., Ferland G. J., Korista K. T., Yakovlev D. G., 1996, ApJ, 465, 487
Wang L., Goodman J., 2017, ApJ, 847, 11 (WG17)
Weber M. L., Ercolano B., Picogna G., Hartmann L., Rodenkirch P. J., 2020, MNRAS, 496, 223

This paper has been typeset from a TEX/LATEX file prepared by the author.